

***Results from Fuel Matrix  
Degradation Model  
Parameterization  
Experiments and Model  
Development Activities***

**Spent Fuel and Waste Disposition**

***Prepared for  
US Department of Energy  
Spent Fuel and Waste Science and  
Technology  
James Jerden  
Sara Thomas  
Eric Lee  
Vineeth Kumar Gattu  
William Ebert  
Argonne National Laboratory  
June 8, 2020  
ANL/CFCT-20/15***

This work was supported by the US Department of Energy, Office of Nuclear Energy. The report was prepared at Argonne National Laboratory as part of the Spent Fuel and Waste Science and Technology Campaign.

**DISCLAIMER**

This information was prepared as an account of work sponsored by an agency of the U.S. Government. Neither the U.S. Government nor any agency thereof, nor any of their employees, makes any warranty, expressed or implied, or assumes any legal liability or responsibility for the accuracy, completeness, or usefulness, of any information, apparatus, product, or process disclosed, or represents that its use would not infringe privately owned rights. References herein to any specific commercial product, process, or service by trade name, trade mark, manufacturer, or otherwise, does not necessarily constitute or imply its endorsement, recommendation, or favoring by the U.S. Government or any agency thereof. The views and opinions of authors expressed herein do not necessarily state or reflect those of the U.S. Government or any agency thereof.

## SUMMARY

This work is being performed as part of the DOE NE Spent Fuel and Waste Science and Technology Campaign, Argillite and Crystalline Rock R&D work packages: SF-20AN01030101 and SF-20AN01030201 respectively. This document is submitted in fulfillment of milestone M4SF-20AN010301013 for Argillite R&D and the milestone M4SF-20AN010302013 for Crystalline R&D.

This report presents results from electrochemical experiments conducted to quantify the corrosion rates of the four most abundant alloys that make up the internal components of a typical spent fuel waste package (316 stainless steel, carbon steel, and aluminum alloy and Zircaloy-4) at several pH values and chloride concentrations. These rates are used to determine the amount of hydrogen gas generated during anoxic corrosion and to parameterize a prototype in-package chemistry (IPC) model that has been integrated with the fuel matrix degradation (FMD) model. The combined model provides spent fuel degradation rates over a range of Eh, pH and chemical conditions relevant for argillite and crystalline rock repository environments.

This model combined model was developed by coupling the FMD model with the reactive transport code X1t, which is a module within the Geochemist's Workbench (GWB) software package. The reactive transport model has been used to calculate the amount of H<sub>2</sub> produced and accumulated within a breached waste package due to the corrosion of stainless steel, carbon steel, aluminum alloys and Zircaloy based on the corrosion rates measured in the experiments discussed in this report. The environmental dependencies of in-package alloy corrosion rates must be taken into account in the FMD model to represent the range of conditions that can occur in a breached waste package. Instantaneous alloy corrosion rates and environmental dependencies (Eh, pH, Cl, T) are needed to calculate the spent fuel degradation rates used to define the radionuclide source term in the GDSA repository performance models. The electrochemical measurements of alloy corrosion rates provide values and dependencies on T, Eh, pH, and Cl<sup>-</sup> conditions that are needed for source term model parameterization and validation for carbon steel and aluminum alloy, which corrode actively, and for 316 stainless steel and Zircaloy-4, which passivate.

The results of this study confirm the conclusions and recommendations that were identified and discussed in Jerden et al., 2017, Jerden et al., 2018 and Jerden et al., 2019. Several of the information gaps identified in those studies remain; however, the present work demonstrates that the electrochemical testing methods employed can be used to address the remaining data needs as discussed in Section 5 below.

This page is intentionally left blank.

## Contents

Acronyms .....	xi
1. INTRODUCTION AND OBJECTIVE .....	1
2. THE FUEL MATRIX DEGRADATION MODEL .....	3
2.1 Fuel Matrix Degradation Model Functionality .....	4
2.2 Breached Waste Package Environment .....	6
3. ELECTROCHEMICAL CORROSION EXPERIMENTS ON IN-PACKAGE ALLOYS: KINETICS OF H <sub>2</sub> GENERATION .....	9
3.1 Hydrogen Producing Reactions.....	9
3.2 Electrochemical Corrosion Test Method .....	10
3.2.1 Comparison of Results from Electrochemical Tests and Coupon Immersion Tests .....	11
3.2.2 Data Analysis Method.....	12
3.3 Results from Electrochemical Corrosion Tests.....	13
3.3.1 AISI 4320 Carbon Steel and Boral.....	15
3.3.2 316 Stainless Steel .....	21
3.3.3 Zircaloy-4.....	29
3.4 Summary of Electrochemical Corrosion Tests.....	34
4. IN-PACKAGE CHEMISTRY SIMULATION AND THE FUEL MATRIX DEGRADATION MODEL: ROLE OF ALLOY CORROSION.....	37
5. CONCLUSIONS AND FUTURE WORK.....	49
5.1 Conclusions.....	49
5.2 Future Work.....	51
6. REFERENCES .....	52

This page is intentionally left blank.

## List of Figures

Figure 1. Flow chart summarizing how the X1t in-package chemistry model and FMD model from this report combine with GDSA-PA models to calculate source term.....	2
Figure 2. Pourbaix diagrams for uranium speciation showing possible range of conditions within a breached waste package due to radiolysis (shaded gray region). This diagram was drawn for a solution with $1 \times 10^{-6}$ molal uranium and $1 \times 10^{-4}$ molal carbonate. Eh is relative to standard hydrogen electrode (SHE).....	3
Figure 3. Schematic diagram showing the conceptual layout and reaction scheme for the fuel matrix degradation model and identifying other key processes that influence in-package chemistry and radionuclide mobilization ( $I_{\text{corr}}$ indicates corrosion current). ....	5
Figure 4. Pourbaix diagram showing the range of possible conditions within a breached waste package due to radiolysis (shaded gray region). ....	6
Figure 5. Conceptual diagram of a generic waste package showing a conceptual canister-breaching scenario. BWR STAD denotes a boiling water reactor standard transport, aging and disposal canister and RN denotes radionuclides (adapted from Energy Solutions, 2015). ....	7
Figure 6. Conceptual diagram of a generic waste package showing a conceptual canister-breaching scenario (adapted from Energy Solutions, 2015). ....	8
Figure 7. Three-electrode electrochemical cell used in Argonne electrochemical experiments (left) and an alloy working electrode (right). ....	10
Figure 8. Conceptual diagram showing how mass loss measurements of steel corrosion rates in immersion tests yield rates that do not represent the corrosion kinetics (adapted from Jerden et al., 2017). ....	12
Figure 9. Potentiostatic tests on AISI 4320 (carbon steel) at pH 10, 0.1 molal NaCl, and 3 fixed potentials ( $V_{\text{SHE}}$ ). ....	16
Figure 10. Potentiostatic test results on Boral at pH 10, 4.3 millimolal NaCl, and various fixed potentials ( $V_{\text{SHE}}$ ). ....	17
Figure 11. Corrosion rates plotted against potentiostatic fixed potentials ( $V_{\text{SHE}}$ ) for AISI 4320 (carbon steel) at pH 10 and various NaCl concentrations overlaid with exponential best-fit lines (Equations 6 – 8). ....	18
Figure 12. Corrosion rates plotted against pH for AISI 4320 (carbon steel) at 4.3 millimolal NaCl concentration and $0.49 V_{\text{SHE}}$ . ....	19
Figure 13. Corrosion rates plotted against pH for AISI 4320 (carbon steel) at pH 10 and $0.49 V_{\text{SHE}}$ (regression line is given in Equation 9). ....	19
Figure 14. Corrosion rates plotted against potentiostatic fixed potentials ( $V_{\text{SHE}}$ ) for Boral at pH 10 and 4.3 millimolal NaCl overlaid with an exponential best-fit line (Equation 10). ....	20
Figure 15. Potentiostatic test results on 316 stainless steel at pH 10, 17 nanomolal NaCl, and various fixed potentials ( $V_{\text{SHE}}$ ). ....	22
Figure 16. Corrosion rates plotted against potentiostatic fixed potentials ( $V_{\text{SHE}}$ ) for 316 stainless steel at pH 4 and various NaCl concentrations overlaid with an exponential best-fit line (Equation 11). ....	23

Figure 17. Corrosion rates plotted against potentiostatic fixed potentials ( $V_{SHE}$ ) for 316 stainless steel at pH 7 and various NaCl concentrations overlaid with an exponential best-fit line. ....	23
Figure 18. Corrosion rates plotted against potentiostatic fixed potentials ( $V_{SHE}$ ) for 316 stainless steel at pH 10 and various NaCl concentrations overlaid with exponential best-fit lines (Equations 13 and 14). ....	24
Figure 20. Corrosion rates plotted against pH for 316 stainless steel at 4.3 nanomolal NaCl concentration. ....	26
Figure 21. Corrosion rates plotted against pH for 316 stainless steel at 0.1 molal NaCl concentration. ....	26
Figure 22. Corrosion rates plotted as a function of NaCl concentration 316 stainless steel at pH 4. ....	27
Figure 23. Corrosion rates plotted as a function of NaCl concentration 316 stainless steel at pH 7. ....	28
Figure 24. Corrosion rates plotted as a function of NaCl concentration 316 stainless steel at pH 10. ....	29
Figure 25. Potentiostatic test results on Zircaloy-4 at pH 10, 0.1 molal NaCl, and various fixed potentials ( $V_{SHE}$ ). ....	31
Figure 26. Corrosion rates plotted against potentiostatic fixed potentials ( $V_{SHE}$ ) for Zircaloy-4 at pH 10 and various NaCl concentrations overlaid with an exponential best-fit line (Equation 17). ....	31
Figure 27. Corrosion rates plotted against pH for Zircaoly at 0.49 $V_{SHE}$ . The trendlines shown are defined in Equations 18 and 19. ....	32
Figure 28. Zircaloy corrosion rates plotted as a function of NaCl concentration. The trendlines are defined in Equations 20 and 21. ....	33
Figure 30. Comparisons of corrosion rate vs. potential ( $V_{SHE}$ ) for 316 stainless steel and Zircaloy-4 at mM NaCl and a range of fixed pH values. The dotted lines indicate the corrosion rates used in the IPC – FMD model sensitivity runs discussed in Section 4 below. ....	35
Figure 31. Flow of information for the coupled X1t prototype in-package chemistry and the FMD model. ....	38
Figure 32. Results from the Case 1 model scenario (Table 7). The time axis refers to the time elapsed from the start of in-package corrosion (assumed to be 1000 years after emplacement). The fuel is assumed to be 1100 years old at time zero in these model runs. In the bottom plot (c), the solid line just below $2 \times 10^{-4} \text{ g m}^{-2} \text{ yr}^{-1}$ is the calculated degradation rate for the Case 1 scenario representing the chemical dissolution rate of the fuel. The dotted lines show the degradation rates calculated for cases with no $\text{H}_2$ for a high burnup fuel (80 GWd/MTU) and a low burnup fuel (30 GWd/MTU). ....	42
Figure 33. Results from the Case 2 and 3 model scenarios (Table 7). The time axis refers to the time elapsed from the start of in-package corrosion (assumed to be 1000 years after emplacement). The points in the middle plot (b) indicate the $\text{H}_2$ concentration thresholds for inhibiting oxidative fuel dissolution for the two different fuel burnups. In the bottom plot (c), the solid line just below $2 \times 10^{-4} \text{ g m}^{-2} \text{ yr}^{-1}$ is the calculated chemical dissolution rate of the fuel. The dotted lines show the degradation rates calculated for cases with no $\text{H}_2$ for a high burnup fuel (80 GWd/MTU) and a low burnup fuel (30 GWd/MTU). ....	43
Figure 34. Results from the Case 4 and 5 model scenarios (Table 7). The time axis refers to the time elapsed from the start of in-package corrosion (assumed to be 1000 years after	



- emplacement). The points in the middle plot (b) indicate the  $H_2$  concentration thresholds for inhibiting oxidative fuel dissolution for the two different fuel burnups. In the bottom plot (c), the solid line just below  $2 \times 10^{-4} \text{ g m}^{-2} \text{ yr}^{-1}$  is the calculated chemical dissolution rate of the fuel. The dotted lines show the degradation rates calculated for cases with no  $H_2$  for a high burnup fuel (80 GWd/MTU) and a low burnup fuel (30 GWd/MTU). .....45
- Figure 35. Results from the Case 6 and 7 model scenarios (Table 7). The time axis refers to the time elapsed from the start of in-package corrosion (assumed to be 1000 years after emplacement). The points in the middle plot (b) indicate the  $H_2$  concentration thresholds for inhibiting oxidative fuel dissolution for the two different fuel burnups. In the bottom plot (c), the solid line just below  $2 \times 10^{-4} \text{ g m}^{-2} \text{ yr}^{-1}$  is the calculated chemical dissolution rate of the fuel. The dotted lines show the degradation rates calculated for cases with no  $H_2$  for a high burnup fuel (80 GWd/MTU) and a low burnup fuel (30 GWd/MTU). .....46
- Figure 36. Results from the Case 8 model scenario (Table 7). The time axis refers to the time elapsed from the start of in-package corrosion (assumed to be 1000 years after emplacement). The points in the middle plot (b) indicate the  $H_2$  concentration thresholds for inhibiting oxidative fuel dissolution for the two different fuel burnups. In the bottom plot (c), the solid line just below  $2 \times 10^{-4} \text{ g m}^{-2} \text{ yr}^{-1}$  is the calculated chemical dissolution rate of the fuel. The dotted lines show the degradation rates calculated for cases with no  $H_2$  for a high burnup fuel (80 GWd/MTU) and a low burnup fuel (30 GWd/MTU). .....47
- Figure 37. Results from the Case 9 model scenario (Table 7). The time axis refers to the time elapsed from the start of in-package corrosion (assumed to be 1000 years after emplacement). The points in the middle plot (b) indicate the  $H_2$  concentration thresholds for inhibiting oxidative fuel dissolution for the two different fuel burnups. In the bottom plot (c), the solid line just below  $2 \times 10^{-4} \text{ g m}^{-2} \text{ yr}^{-1}$  is the calculated chemical dissolution rate of the fuel. The dotted lines show the degradation rates calculated for cases with no  $H_2$  for a high burnup fuel (80 GWd/MTU) and a low burnup fuel (30 GWd/MTU). .....48

## List of Tables

Table 1. Current densities and corrosion rates from electrochemical corrosion tests on AISI 4320 (carbon steel) and Boral.....	15
Table 2. Current densities and corrosion rates from electrochemical corrosion tests on 316 stainless steel .....	21
Table 3. Current densities and corrosion rates from electrochemical corrosion tests on Zircaloy-4 .....	30
Table 4. Empirical functions (Equations 6 – 21) derived from the potentiostatic test results discussed in Section 3.3.....	36
Table 5. Alloy masses and specific surface areas used in the X1t in-package chemistry model (values are from CRWMS, 2003).....	37
Table 6. Initial solution composition used in X1t in-package chemistry model (from Fernandez et al., 2007). This composition is typical pore-water from the Opalinus clay.....	37
Table 7. Conditions for sensitivity runs performed using the linked X1t IPC and FMD models. The corrosion rates chosen for these model runs span the range of rates measured in the electrochemical tests discussed in Section 3 above. ....	40

## ACRONYMS

BWR	Boiling Water Reactor
DOE	U.S. Department of Energy
EIS	Electrochemical impedance spectroscopy
FEPs	Features, events, and processes
FMD	Fuel matrix degradation (model)
FMDM	Fuel matrix degradation model
FP	Fission product
GDSA	Geologic Disposal Safety Assessment
GWB	Geochemist's Workbench
IPC-FMD	In-package chemistry-fuel matrix degradation (model)
NMP	Noble metal particle
PA	Performance assessment
RN	Radionuclide
SEM	Scanning electron microscopy
SHE	Standard hydrogen electrode
SFWS	Spent Fuel and Waste Science and Technology (campaign)
SF	Spent fuel
STAD	Standardized Transportation, Aging and Disposal Canister

This page is intentionally left blank.

## 1. INTRODUCTION AND OBJECTIVE

The purpose of this project is to develop, test and implement a process model that provides the degradation rate of spent nuclear fuel under a wide range of conditions that can be readily incorporated into the geologic disposal safety assessment (GDSA) performance assessment (PA) code to provide reliable radionuclide source terms over the service life of a deep geologic repository. The fuel matrix degradation (FMD) model described herein was developed for this purpose and is currently being updated, optimized and tested. The FMD model is an electrochemical reactive-transport model built using fundamental redox kinetics and thermodynamics. It is based on the Canadian Mixed Potential Model (CMPM) of Shoesmith and King, 1998, Shoesmith et al., 2003 and King and Kolar 2003 but quantifies the attenuating effect of  $H_2$  on the spent fuel degradation rate and has been customized for application in the ongoing spent fuel and waste science and technology (SFWS) campaign.

The continuing development and implementation of the FMD model addresses two high level Features, Events, and Processes (FEPs) that are recognized as high R&D priorities for the SFWS campaign (Wang et al., 2014). The addressed FEPs include 2.1.02 (waste form) and 2.1.03 (waste container), which correspond to the high priority research topics P19 (Development of waste form degradation model) and P20 (Development of new waste package concepts and models for evaluation of waste package performance for long-term disposal) identified by Wang et al., 2014.

Specifically, the FMD model employs mixed potential theory to calculate the degradation rate of  $UO_2$  by accounting for all major interfacial anodic and cathodic reactions. The major phenomena included in the FMD model are:

- Hydrogen ( $H_2$ ) production from steel corrosion within a breached waste package,
- Alpha radiolysis and radiolytic oxidant (e.g.,  $H_2O_2$ ) generation as a function of fuel burn-up,
- Growth of a porous layer of uranyl oxyhydroxide and/or uranyl peroxide corrosion phases,
- Complexation of dissolved uranium by carbonate,
- Temperature variations of reaction rates,
- One-dimensional diffusion of all chemical species to and from the fuel and steel surfaces,
- Bulk solution reactions such as the oxidation of ferrous iron by  $O_2$  and radiolytic  $H_2O_2$ .

The most important process included in the FMD model that was not addressed in the original CMPM is the oxidation of dissolved  $H_2$  at the spent fuel surface (Jerden et al., 2015). The  $H_2$  generated by steel corrosion in leaching experiments with spent fuel and simulated spent fuel has been seen to decrease the fuel degradation rate by as much as three orders of magnitude compared to the same tests performed in the absence of steel (e.g., Rölliin et al., 2001, Ollila, 2008). How this  $H_2$  effect is represented in the FMD model is discussed in Section 2 below.

Jerden et al., 2017 discussed including a corroding steel surface as a source of  $H_2$  in the FMD model (FMDM version 3). One notable finding from that work is the extensive coupling between the corrosion of waste package components and the corrosion of spent fuel, which must be taken into account to accurately predict radionuclide source terms. As discussed in Jerden et al., 2017, the Eh and pH conditions within a breached waste package will evolve with time due to the coupled reactions of alloy corrosion, radiolysis, and spent fuel dissolution.

Depending on the waste package design, various waste package components will be in electrical contact when contacted by seepage water. Galvanic coupling and galvanically-induced corrosion will affect the dissolution rates of the individual waste components: the corrosion rate of the most susceptible component (which serves as the anode) will be accelerated and corrosion of the more noble component(s) (serving as

the cathode) will decrease. In this study, initial tests were conducted to measure the behaviors of the individual materials as they equilibrated under various test conditions. Future tests will be performed to measure corrosion rates of various coupled systems using a recently developed method. This will permit modeling of various waste package designs. Implementation of the metal corrosion model with the FMD model is demonstrated here by using rates measured for individual metals. More extensive experimental and modeling work is needed to accurately represent the dynamics of in-package chemistry, galvanically-induced alloy corrosion, and fuel degradation.

In Jerden et al., 2019, we discussed ongoing experimental work to measure the corrosion rates of waste package alloys and the parameterization of this information for use in the latest version of the FMD model (FMDM version 4). Here, we discuss electrochemical experiments that are being performed to parameterize the FMD model (V.4).

As summarized in Jerden et al., 2019, the FMD model has been successfully integrated with the GDSA-PA code PFLOTRAN. The flow of information within the integrated FMDM – GDSA-PA model is summarized in Figure 1. The prototype in-package chemistry (IPC) model identified in Figure 1 has been implemented in the reactive transport code X1t, which is a module within the Geochemist's Workbench software package. This IPC model is referred to as a “prototype” because it is anticipated that a different version of the in-package chemistry model will be required to facilitate integration with other GDSA process models (including the FMD model).

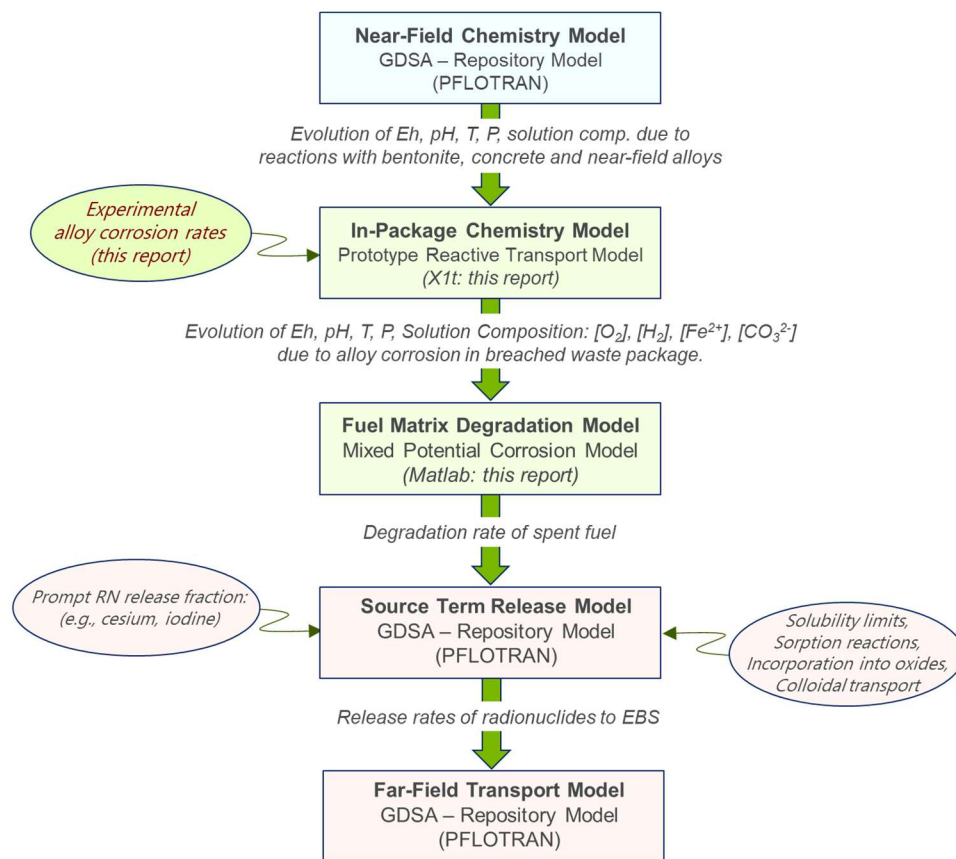


**Figure 1.** Flow chart summarizing how the X1t in-package chemistry model and FMD model from this report combine with GDSA-PA models to calculate source term.

## 2. THE FUEL MATRIX DEGRADATION MODEL

The FMD model is based on fundamental electrochemical principals, mixed potential theory, and traditional mass balance and reactive transport relationships (King and Kolar, 1999) to determine the degradation rate of the fuel. Specifically, the FMD model calculates the dissolution rate of spent fuel as a function of the interfacial corrosion potential ( $E_{\text{corr}}$ ), at which all of the anodic and cathodic half reactions occurring at the fuel/solution boundary are kinetically balanced with no net electron transfer. The dissolution rate (which corresponds to an anodic current due to the oxidation of  $\text{U}^{4+}$  to  $\text{U}^{6+}$ ) is relatively high under oxidizing conditions above the U(IV)/U(VI) threshold potential, but significantly lower at potentials where only solubility-limited chemical dissolution of  $\text{U}^{4+}$  occurs.

The threshold potential for U(IV)/U(VI) oxidative dissolution depends on pH, as shown in Figure 2, and on the water chemistry. Under the reducing conditions envisioned in argillite and crystalline rock repositories, the Eh of the solution is expected to be below  $-0.1 \text{ V}_{\text{SHE}}$  between pH 7 – 9 (Laaksoharju et al., 2008), which is well below the U(IV)/U(VI) threshold. However, the radiolysis of water by spent fuel to form  $\text{H}_2\text{O}_2$  and other radiolytic oxidants can cause localized oxidizing conditions that drive the Eh far above the threshold for oxidative dissolution of the fuel, i.e., into the U(VI) stability field. The shaded area in Figure 2 shows the possible range of in-package conditions due to radiolysis. Thus, the FMD model must have the capability to address a pH range from about 4 to 11 and Eh values spanning the range of water stability.

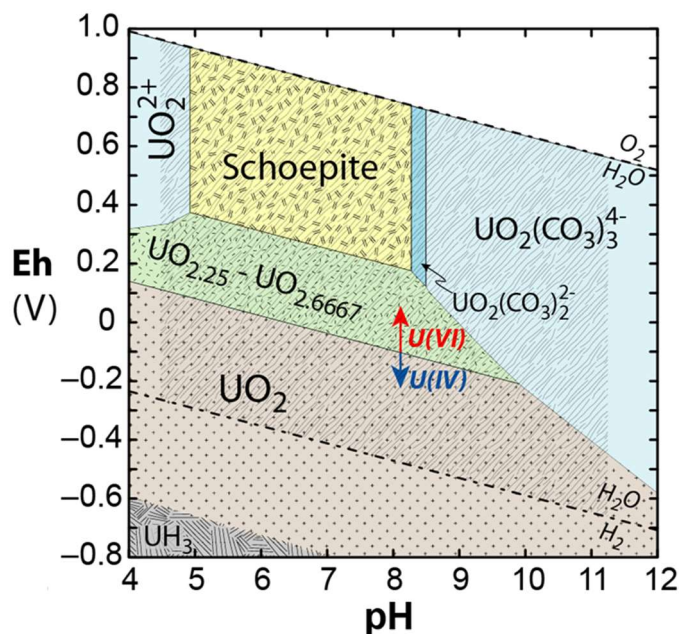


**Figure 2.** Pourbaix diagrams for uranium speciation showing possible range of conditions within a breached waste package due to radiolysis (shaded gray region). This diagram was drawn for a solution with  $1 \times 10^{-6}$  molal uranium and  $1 \times 10^{-4}$  molal carbonate. Eh is relative to standard hydrogen electrode (SHE).

A number of experimental and modeling studies have shown that the oxidative dissolution of spent fuel in anoxic environments is counteracted by the catalyzed oxidation of  $\text{H}_2$  on fission product alloy phases referred to as the Ru  $\epsilon$ -phase or noble metal particles (NMP) (e.g., Broczkowski et al., 2005, Shoesmith, 2008, Grambow, et al., 2010). This phenomenon, which we refer to as the  $\text{H}_2$  effect, has been reported to decrease spent fuel dissolution rates by up to 3 orders of magnitude in comparison to the maximum

dissolution rates attained in the absence of  $H_2$  (e.g., Röllin et al., 2001, Ollila, 2008). The major goal of the ongoing FMD model development work is to implement an accurate model that quantifies the generation and accumulation of  $H_2$  and its influence on spent fuel degradation rates.

Two main sources of  $H_2$  in the repository will be: (1) the radiolysis of in-package solutions, and (2) the anoxic corrosion of steels and other alloys present within the breached waste package and in the surrounding EBS and nearfield. Of these  $H_2$  sources, alloy corrosion has been shown to be, by far, the most important (e.g., Johnson and King, 2003, Turnbull, 2009). Therefore, we must account for alloy corrosion within a breached waste package to accurately represent the effect of  $H_2$  on spent fuel degradation rates. To this end, the FMD modeling work has expanded to include the quantification of alloy corrosion as a source of  $H_2$  (e.g., Jerden et al., 2017, Jerden et al., 2018, Jerden et al., 2019).

Our on-going work addresses the coupling between the corrosion of waste package components and the spent  $UO_2$  fuel. As shown in Jerden et al., 2017 and Jerden et al., 2019, the Eh and pH conditions within a breached waste package will evolve with time due to coupled reactions of alloy corrosion, radiolysis, and spent fuel dissolution. The latest FMD model accounts for radiolysis and takes a step towards accounting for coupled processes by linking alloy corrosion kinetics and fuel degradation rates. However, more experimental and modeling work is needed to more accurately model the dynamic relationship between spent fuel degradation and in-package alloy corrosion.

## 2.1 Fuel Matrix Degradation Model Functionality

The key processes represented in the latest version of the FMD model include:

- The generation of radiolytic oxidants as a function of fuel burn-up,
- The NMP ( $\epsilon$ -phase)-catalyzed oxidation of  $H_2$ , which protects the fuel from oxidative dissolution,
- The precipitation and growth of a uranyl oxyhydroxide (schoepite) corrosion layer that blocks radiolysis at the fuel/solution interface and slows the diffusion of reactants to and from the fuel surface,
- The complexation of uranyl by carbonate,
- The destruction of  $O_2$  and radiolytic  $H_2O_2$  by ferrous iron within the bulk solution,
- Temperature variations of reaction rates (by Arrhenius equations),
- The one-dimensional diffusion of all chemical species to and from the fuel and steel surfaces,
- The anoxic corrosion of alloy components to generate dissolved  $H_2$  and oxidized metals (e.g., ferrous iron from steel).

As discussed above, the effect of  $H_2$  oxidation is the most important of the above processes for determining the fuel dissolution rate and the radionuclide source terms (Jerden et al. 2015). The second most important effect is the oxidative dissolution of the fuel by the radiolytic oxidant  $H_2O_2$  and its decomposition product  $O_2$ . In the FMD model, the  $H_2O_2$  concentration is calculated using an analytical form of the radiolysis model developed at PNNL (Buck et al., 2014) and a burn-up/dose rate function derived from Radulescu, 2011.

The layout and reaction scheme of the FMD model is shown in Figure 3.



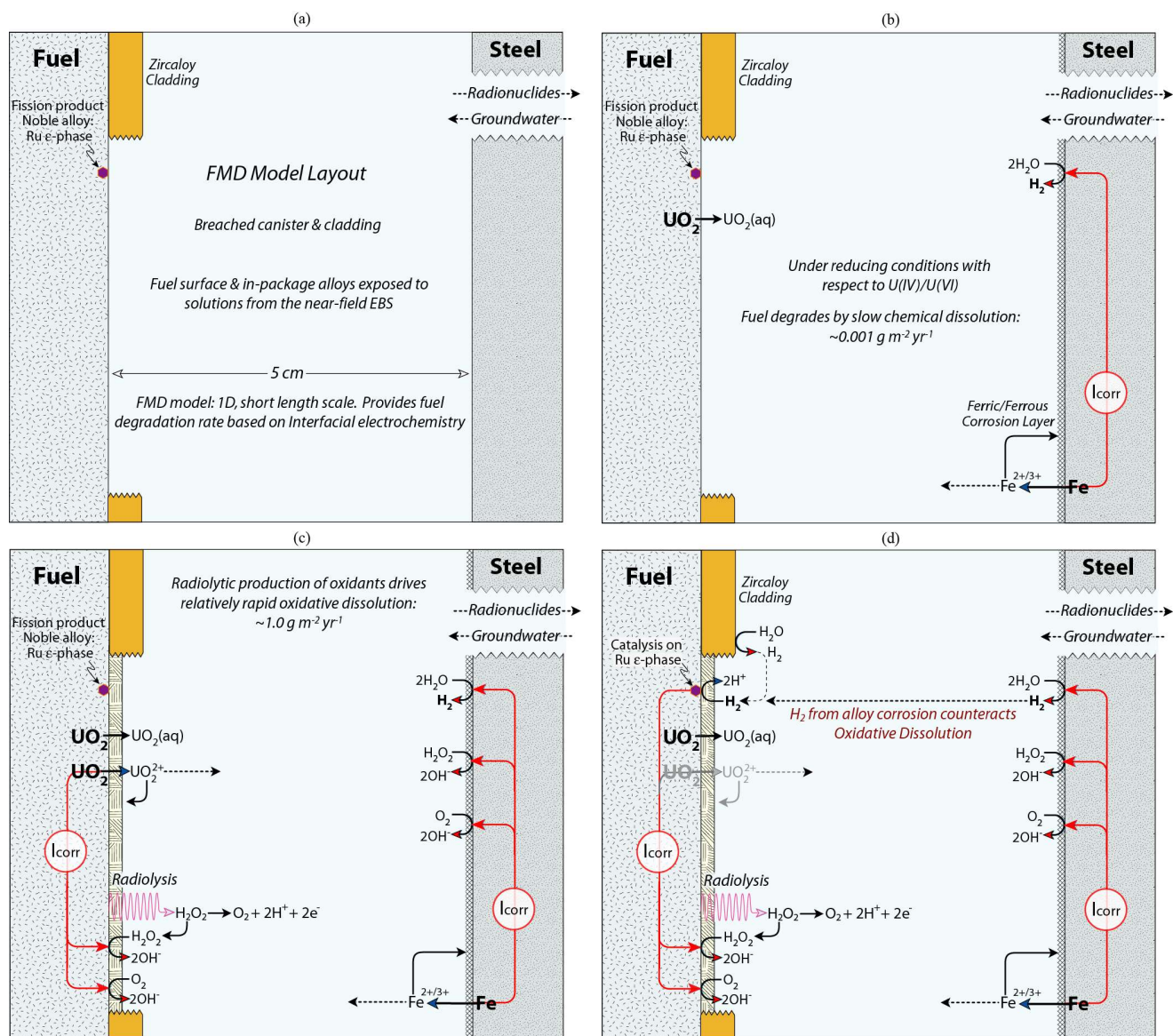


**Figure 3.** Schematic diagram showing the conceptual layout and reaction scheme for the fuel matrix degradation model and identifying other key processes that influence in-package chemistry and radionuclide mobilization ( $I_{corr}$  indicates corrosion current).

The steps involved in radionuclide release from spent fuel that are or will be represented in the FMD model are as follows:

- In a breached waste package, groundwater will infiltrate open spaces within the canister and begin to corrode in-package alloys.
- Alloy corrosion will produce  $H_2$  even when the infiltrating groundwaters are electrochemically reducing with respect to the fuel. This is because the stability fields of carbon steels and stainless steels lie below the stability field of water, as shown in Figure 4.
- Assuming that the Zircaloy cladding has also been breached, the fuel will begin degrading when contacted by seepage water by either relatively rapid oxidative dissolution ( $\sim 1 - 10 \text{ g/m}^2 \text{ yr}$ ) or by

- 

## 2.2 Breached Waste Package Environment

Simplified conceptual diagrams of a typical spent fuel waste package in a generic crystalline or argillite repository setting are shown in Figures 5 and 6 (adapted from Energy Solutions, 2015). These figures highlight the spatial arrangement of waste package components and key processes that the FMD model represents. As shown in Figures 5 and 6, the spent fuel assemblies will be surrounded by (and in close contact with) a number of alloy components within the waste package. These materials include carbon steel (C-steel), 316 stainless steel (316SS) and either borated aluminum or borated steel alloys. Another important material from the prospective of H<sub>2</sub> production in the repository is the Zircaloy cladding retaining the fuel pellets (gold or yellow in Figures 5 – 6). Although Zircaloy is not considered as a barrier to radionuclide release in the current FMD or GDSA PA models, Zircaloy corrosion could be an important source of H<sub>2</sub> and should be included in the FMD model. Quantifying the effect of Zircaloy corrosion in the FMD model is a subject of ongoing model development work.



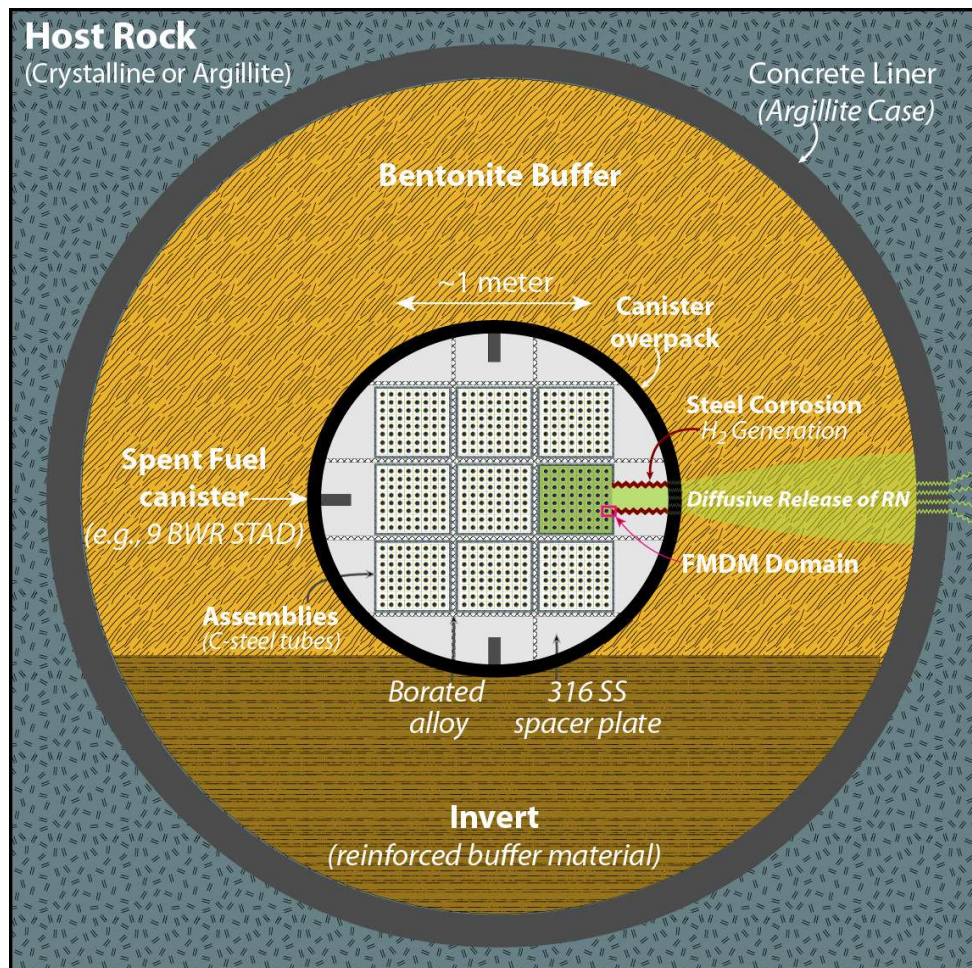


**Figure 5.** Conceptual diagram of a generic waste package showing a conceptual canister-breaching scenario. BWR STAD denotes a boiling water reactor standard transport, aging and disposal canister and RN denotes radionuclides (adapted from Energy Solutions, 2015).

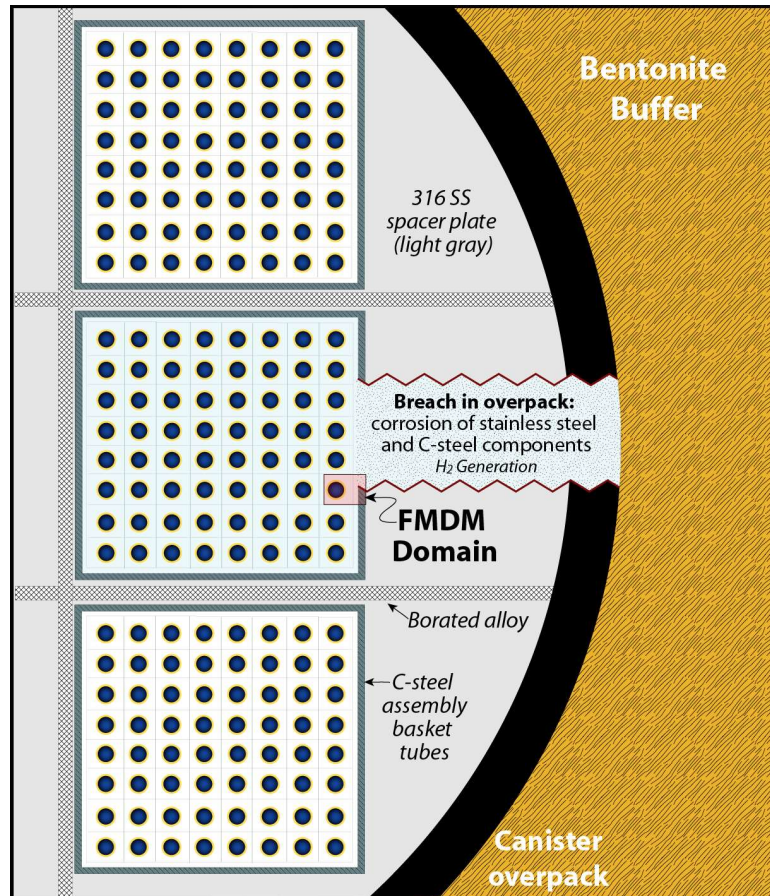


**Figure 6.** Conceptual diagram of a generic waste package showing a conceptual canister-breaching scenario (adapted from Energy Solutions, 2015).

### 3. ELECTROCHEMICAL CORROSION EXPERIMENTS ON IN-PACKAGE ALLOYS: KINETICS OF H<sub>2</sub> GENERATION

#### 3.1 Hydrogen Producing Reactions

Accurate alloy corrosion rates that are measured under relevant disposal conditions are essential to model source term due to the dominant effect that H<sub>2</sub> produced from alloy corrosion has on the spent fuel dissolution rate (as discussed in Section 2). The half-cell reactions of particular interest for H<sub>2</sub> generation during the oxidation of relevant alloys are as follows:



with the overall steel corrosion reactions



Analogous reactions can be written for zirconium and aluminum alloys:



Reactions 4 - 7 provide the fundamental coupling between alloy corrosion and H<sub>2</sub> generation. The oxidation of minor alloy constituents (Cr, Mo, Ni, and Mn in steel and Sn in Zircaloy) will also contribute to the anodic current, but the oxidation of Fe (in steel), Al (in Boral), and Zr (in Zircaloy) will be dominant.

As discussed in Jerden et al., 2017, there is a wealth of literature on steel corrosion, but much of the previous work was not done under repository-relevant conditions. Studies that did use relevant solutions, such as bentonite pore waters (see reviews by Johnson and King, 2003 and King, 2007), involved batch style immersion tests that provided average cumulative rates rather than the instantaneous corrosion rates needed to parameterize and validate the in-package chemistry model.

Steel coupon immersion tests provide valuable information on the corrosion product mineralogy and the evolution of the chemical system. However, corrosion rates derived from immersion tests are based on cumulative mass loss measurements or corrosion layer thicknesses that do not indicate how the corrosion rate (and thus H<sub>2</sub> generation rate) varies with time or conditions (most importantly, with the solution Eh). Knowing these dependencies of the H<sub>2</sub> generation rate is essential for modeling spent fuel dissolution under evolving in-package chemical conditions.

During an immersion test with a passivating steel, most of the mass loss occurs before the steel surface is passivated. This may skew the average rate to high values. We need to know how the instantaneous corrosion rate controlling the H<sub>2</sub> generation changes as the conditions evolve to accurately represent the flux of H<sub>2</sub> in the FMD model. Electrochemical techniques allow us to measure instantaneous rates under carefully controlled chemical and redox conditions. This is discussed further in Section 3.2.1.



Electrochemical tests also quantify the effects of surface stabilization due to passivation and localized corrosion (such a pitting) that can only be qualitatively observed in coupon immersion tests. Furthermore, electrochemical methods can measure rates on the order of  $10^{-3} \text{ g m}^{-2} \text{ yr}^{-1}$  ( $10^{-4} \text{ } \mu\text{m yr}^{-1}$ ). Therefore, electrochemical methods yield reliable corrosion rates for durable EBS materials (including 316 stainless steel and Zircaloy cladding) and provide dependencies on environmental conditions needed to predict the long-term generation of  $\text{H}_2$  and attenuation of fuel degradation rates as the seepage water composition evolves.

### 3.2 Electrochemical Corrosion Test Method

The electrochemical corrosion experiments employ the standard three electrode method as described by Bard and Faulkner, 2001. The three-electrode cell used for the tests at Argonne consists of a 20 mL jacketed, borosilicate glass vessel with a mercury/mercurous sulfate reference electrode, a graphite counter electrode and a working electrode consisting of the alloy to be tested. A typical electrochemical cell and working electrode is shown in Figure 7. The voltages reported herein have been adjusted to the standard hydrogen electrode (SHE), which is the reference used in the FMD model.

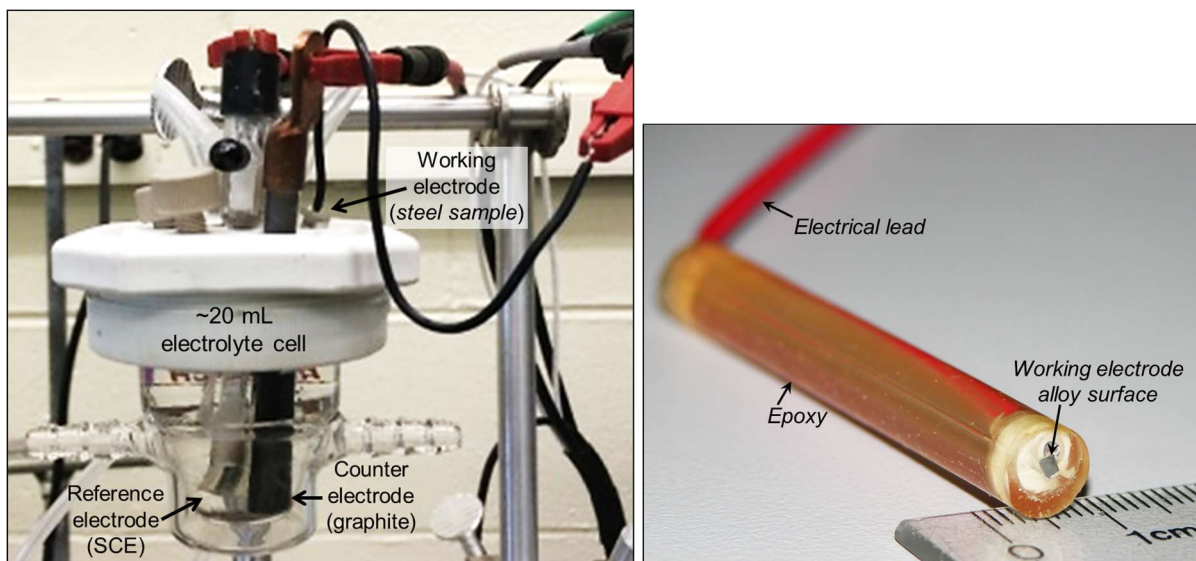


**Figure 7.** Three-electrode electrochemical cell used in Argonne electrochemical experiments (left) and an alloy working electrode (right).

In the electrochemical tests, the composition of the electrolyte is used to impose chemical effects, including pH,  $\text{Cl}^-$  concentration, and other solutes of interest, and a potentiostat is used to impose several surface potentials of interest, which can be significantly different than the Eh of the solution used in the test. The potentiostat allows a wide range of potentials to be applied to efficiently determine the effect of the solution redox (Eh) on the alloy corrosion and  $\text{H}_2$  generation rates under controlled chemical conditions. In practice, a potentiodynamic scan is performed to measure the corrosion potential ( $E_{\text{corr}}$ ) for the polished surface in the test solution and identify regions of active and passive behavior to be studied in subsequent potentiostatic tests. Several potentiostatic tests are conducted at voltages selected to measure the corrosion currents after stable passive layers have formed on passivating metals or after stable currents have been achieved by actively corroding metals. A stable current indicates that the surface has equilibrated under the

test conditions (pH, chloride concentration, temperature, applied potential) and is interpreted to represent the long-term corrosion rate under those conditions.

### 3.2.1 Comparison of Results from Electrochemical Tests and Coupon Immersion Tests

As discussed in Jerden et al., 2017, there are many studies in the literature addressing steel corrosion, but much of the previous work was not done under repository-relevant conditions. The studies that were done using relevant solutions, such as bentonite pore waters (see reviews by Johnson and King, 2003 and King, 2007), involved batch style immersion tests that provided average cumulative rates rather than the instantaneous corrosion rates needed to parameterize and validate the FMD model. The instantaneous corrosion rate refers to the oxidation reactions that result in the generation of  $H_2$ . The FMD model tracks the kinetics for diffusion of the generated  $H_2$  to the fuel surface and its subsequent oxidation on noble metal particles.

The immersion tests quantify the cumulative extent of corrosion (based on the specimen mass loss or thickness of the corrosion layer) that occurs over a given test duration; they do not provide the instantaneous corrosion rates needed to determine  $H_2$  generation rates (see Jerden et al., 2017). The difference between the cumulative rates from immersion tests and the instantaneous rates measured electrochemically is illustrated in Figure 8 (adapted from Jerden et al., 2017), where the blue curve represents the actual mass of a passivating metal such as 316 stainless steel that is oxidized during a coupon corrosion test. The blue curve shows that the majority of corrosion occurs prior to passive stabilization and little further corrosion occurs after that. At the end of the immersion test duration, the oxide layer is carefully removed, and the corroded coupon is weighed to determine the mass lost due to corrosion; two blue circles are included in Figure 8 to represent the extents of corrosion measured after two durations. The two tests only provide the average corrosion rates indicated by the dashed green lines in Figure 9 after those test durations. The corrosion behavior is not well-represented by the cumulative rates, which give an “artificial” dependence on the test duration. That is, the average rate will decrease with longer test durations even though most of the mass loss occurred early in the test.

The instantaneous rate of corrosion (which determines the  $H_2$  generation rate at each point in time) is given by the slope of the blue curve. That rate decreases significantly after the surface passivates and becomes much lower than the average cumulative rate. In principle, an extensive series of immersion tests could be conducted for different durations to derive the mass loss curve, but the mass loss of a passivated surface will be too small to measure. Regardless, immersion test results do not indicate the dependence of the corrosion rate on the solution Eh that is needed for the FMD model. Immersion tests can only provide corrosion rates under the test conditions, which will drift as the solutions and specimen surfaces evolve. The electrochemical method employed for this study directly measures the metal oxidation rates needed to calculate  $H_2$  generation rates in the FMD model under wide ranges of controlled redox and test conditions (Eh, pH, chloride concentrations).

The electrochemical tests can measure oxidation rates on the order of  $10^{-3} \text{ g m}^{-2} \text{ yr}^{-1}$  ( $10^{-4} \text{ } \mu\text{m yr}^{-1}$ ) and quantify the effects of localized corrosion processes, such as pitting, and surface passivation on the corrosion rate. The electrochemical method provides reliable corrosion rates for durable EBS materials (including Zircaloy cladding) over the wide range of environmental conditions that could occur in a breached waste package that are needed to predict the generation of  $H_2$ .

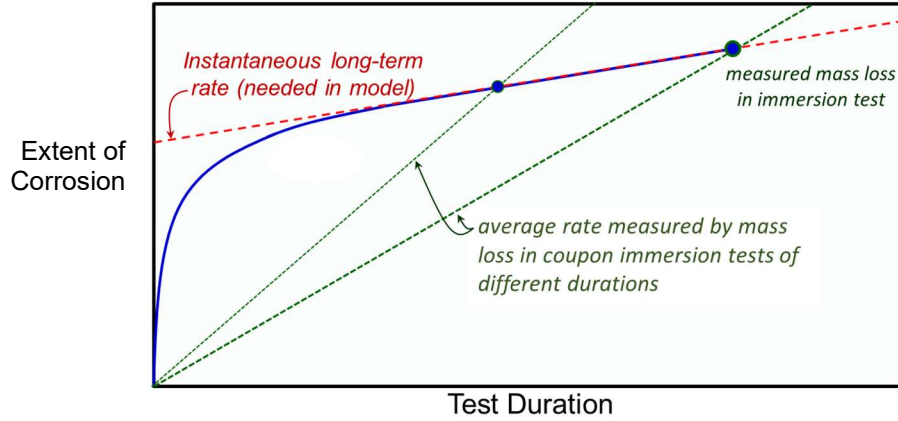


**Figure 8.** Conceptual diagram showing how mass loss measurements of steel corrosion rates in immersion tests yield rates that do not represent the corrosion kinetics (adapted from Jerden et al., 2017).

### 3.2.2 Data Analysis Method

Potentiostatic tests are conducted to monitor the current as the material surface interacts with the solution, which may result in passivation or active corrosion. In most cases, a steady current is achieved within a few days and indicates a constant corrosion rate. The steady current densities measured in the potentiostatic test are converted directly into alloy corrosion rates by using Faraday's Law which relates the cumulative charge transferred through the working electrode to the mass of metal oxidized during an experiment (Equation 1). Since the cumulative charge transferred is a function of the reaction current over time (Equation 2) we can use current densities measured during potentiostatic tests to calculate corrosion rates (Equations 3 and 4)

$$m = \frac{QM}{nF} \quad \text{Equation 1}$$

where  $m$  is the mass of substance oxidized,  $Q$  is the total electric charge passed through the electrode substance,  $M$  is the molecular weight of the electrode substance,  $F$  is the Faraday constant, and  $n$  is the number of electrons transferred.

The cumulative electric charge  $Q$  is the integrated reaction current measured at the electrode:

$$Q = \int_0^t I(t) dt \quad \text{Equation 2}$$

Where  $I(t)$  is the reaction current measured at the electrode at time  $t$ . Therefore, the mass of material oxidized at the electrode surface can also be calculated from the measured reaction current at the electrode. If the corrosion current is constant, the mass corroded over an interval  $\Delta t$  can be calculated as:

$$m = \frac{I \cdot \Delta t \cdot M}{nF} \quad \text{Equation 3}$$

and the rate can be calculated as

$$\text{rate} = \frac{m}{\Delta t} = \frac{IM}{nF} \quad \text{Equation 4}$$



The current and mass released can be normalized to the surface area of the electrode to give corrosion rates in units of  $\text{g m}^{-2} \text{yr}^{-1}$ , which can be converted to penetration rates in  $\text{mm yr}^{-1}$  using the density of the steel. It also gives the  $\text{H}_2$  generation rate using the stoichiometry of Reactions 4 – 7 shown above.

Each electrochemical experiment involves the following sequence of steps:

- Electrochemical cleaning at a potential far below the corrosion potential of the material to remove any native oxide from the sample electrode,
- Potentiodynamic scans to determine  $E_{\text{corr}}$  of alloy under chemical conditions of interest,
- Potentiostatic holds (up to 8 days) at several relevant redox conditions to quantify effects of passivation,
- Periodic electrical impedance spectroscopy analyses to characterize the evolving properties of corroded surface,
- Detailed microscopy (reflected light, SEM/EDS) to characterize changes in alloy microstructures during test.

The results from these tests provide the following information:

- Corrosion rates for surfaces equilibrated under controlled environmental conditions,
- Electrical properties of the passivated surfaces to provide confidence in their long-term stability,
- Data to derive analytical expressions for key corrosion rate dependencies (Eh, pH, chloride concentration) to calculate evolution of  $\text{H}_2$  concentrations in breached waste package,
- Corrosion products for further analyses.

The Butler-Volmer equation (as defined by Bard and Faulkner, 2001) relates the anodic current density to the applied over-potential as:

$$j_a = j_0 \cdot \exp\left(\frac{(1-\alpha) \cdot z \cdot F}{(R \cdot T)} (E - E_{eq})\right) \quad (\text{Equation 5})$$

where  $j_a$  is the anodic current density ( $\text{A m}^{-2}$ ),  $j_0$  is the exchange current density ( $\text{A m}^{-2}$ ),  $\alpha$  is the charge transfer coefficient,  $z$  is the number of electrons involved in the corrosion reaction,  $F$  is the Faraday constant,  $R$  is the universal gas constant,  $T$  is absolute temperature,  $E_{eq}$  is the equilibrium electrode potential ( $E_{\text{corr}}$ ) and  $E$  is the instantaneous electrode potential applied during the test. The Butler-Volmer equation is typically restricted to deviations from less than 0.2 V and the high applied potentials used to represent the range of conditions that could occur in a disposal system will likely result in deviations from Butler – Volmer behavior. The added effects of high pH and chloride concentrations may also lead to deviations. The dependencies can be represented using empirical relationships determined by plotting corrosion rate as a function of applied potential, pH, and chloride concentration. This approach allows us to define the analytical functions needed in the X1t in-package chemistry model to predict the  $\text{H}_2$  generation rates (from alloy corrosion) over the wide range of relevant Eh and pH conditions to be input into the FMD model. The empirical dependencies of the alloy corrosion rates on pH and chloride are quantified in Section 3.3.

### 3.3 Results from Electrochemical Corrosion Tests

The test conditions and results from the electrochemical corrosion tests are shown in Tables 1 - 3 and the data trends are shown in Figures 9 - 30.

The effects of Eh, as represented by the applied potentials in the potentiostatic tests, are quantified in the IPC – FMD model using an exponential dependence consistent with the form of the Butler-Volmer equation (Equation 5). Preliminary empirical relationships for the effects of pH and chloride concentration on the alloy corrosion rates are being derived for data sets showing regular trends (Equations 6 – 21). Exponential functions provide reasonable quantitative descriptions of the data under most experimental conditions (Figures 11, 14, 16, 17, 18, and 26), though many deviations are not yet understood. Future experimental work will aim to better quantify the combined effects to provide more accurate analytical functions that quantify the alloy corrosion rate dependence on Eh, pH, chloride and temperature.

### 3.3.1 AISI 4320 Carbon Steel and Boral

The results for AISI 4320 carbon steel and Boral corrosion under different test conditions are provided in Table 1. Both the experimentally measured current densities (CD) and calculated corrosion rates (CR) are provided. A few corrosion tests that were run at potentials of  $-0.06 V_{SHE}$  and lower had net cathodic currents (i.e., negative values), indicating that the test potentials were lower than  $E_{corr}$  under those conditions. (Note that the value of  $E_{corr}$  increases as the surface passivates.) The cathodic currents indicate the rate of cathodic reactions catalyzed by the metal surface, including  $H_2$  formation (Reaction 3 above).

**Table 1.** Current densities and corrosion rates from electrochemical corrosion tests on AISI 4320 (carbon steel) and Boral

Alloy	pH	NaCl (molal)	Quantity*	Volts vs. SHE					
				0.49	0.24	-0.06	-0.26	-0.44	-0.66
4320 (C-steel)	4	4.3E-03	CD	1.2E-02	----	----	----	----	----
			CR	1.1E+06	----	----	----	----	----
	7	4.3E-03	CD	1.4E-03	----	----	----	----	----
			CR	1.2E+05	----	----	----	----	----
	10	1.7E-09	CD	3.8E-07	1.9E-07	-6.6E-06	----	----	----
			CR	3.5E+01	1.7E+01	Cathodic	----	----	----
		4.3E-03	CD	1.5E-03	----	-1.7E-06	----	7.7E-05	-2.5E-05
			CR	1.4E+05	----	Cathodic	----	7.0E+03	Cathodic
		1.0E-01	CD	1.1E+00	1.5E-02	9.3E-04	----	----	----
			CR	9.7E+07	1.4E+06	8.5E+04	----	----	----
Boral	10	4.3E-03	CD	1.5E-03	5.8E-04	----	1.4E-04	----	----
			CR	4.4E+04	1.7E+04	----	4.2E+03	----	----

\*CD = current density ( $A\ cm^{-2}$ ), CR = Corrosion Rate ( $g\ m^{-2}\ yr^{-1}$ ), ---- = not measured.

The lowest carbon steel corrosion rate measured was  $1.7\ g\ m^{-2}\ yr^{-1}$  for the test with 17 nanomolal NaCl,  $0.24 V_{SHE}$ , and pH 10, while the highest carbon steel corrosion rate measured was  $9.7 \times 10^7\ g\ m^{-2}\ yr^{-1}$  at 100 millimolal NaCl,  $0.49 V_{SHE}$ , and pH 10. The measured corrosion rates of carbon steel strongly depend on the concentration of NaCl. The effect of pH on the corrosion rate of carbon steel is not as significant as NaCl concentration. When NaCl is 4.3 millimolal and the potential is held at  $0.49 V_{SHE}$ , the corrosion rate is highest at pH 4 ( $1.1 \times 10^6\ g\ m^{-2}\ yr^{-1}$ ) and approximately an order of magnitude lower at both pH 7 and pH 10.

Figure 9 presents selected potentiostatic scans from carbon steel experiments at pH 10, 0.1 molal NaCl, and potentials ranging from 0.49 V<sub>SHE</sub> to -0.26 V<sub>SHE</sub>. The current densities in these scans remain high and do not reach clearly stable values at the positive hold potentials in Figure 9. The high current densities are attributed to the lack of passivation for this alloy (the magnetite corrosion product layers are porous and do not electrochemically protect the alloy surface from future corrosion).

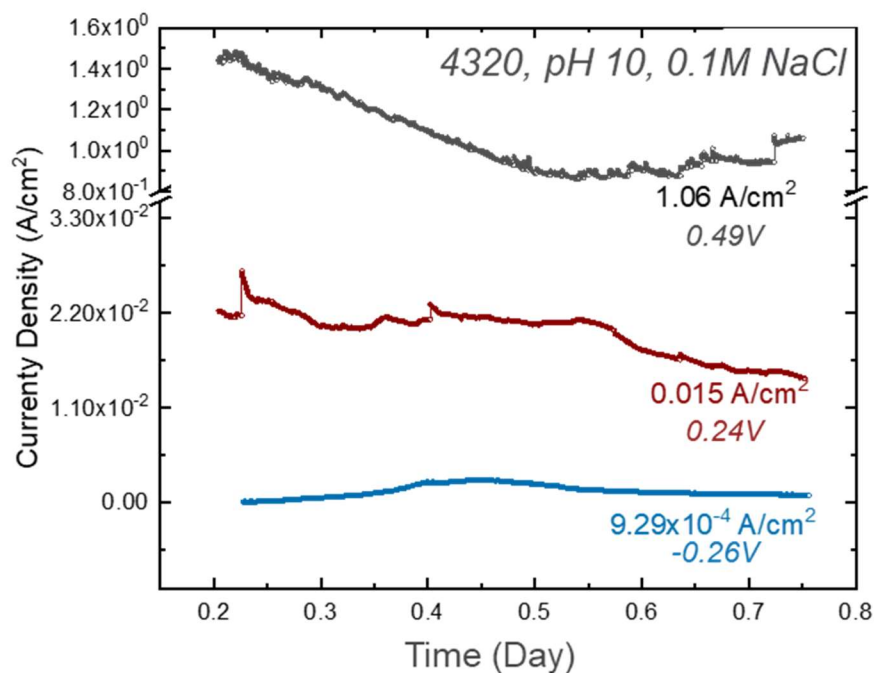


**Figure 9.** Potentiostatic tests on AISI 4320 (carbon steel) at pH 10, 0.1 molal NaCl, and 3 fixed potentials (V<sub>SHE</sub>).

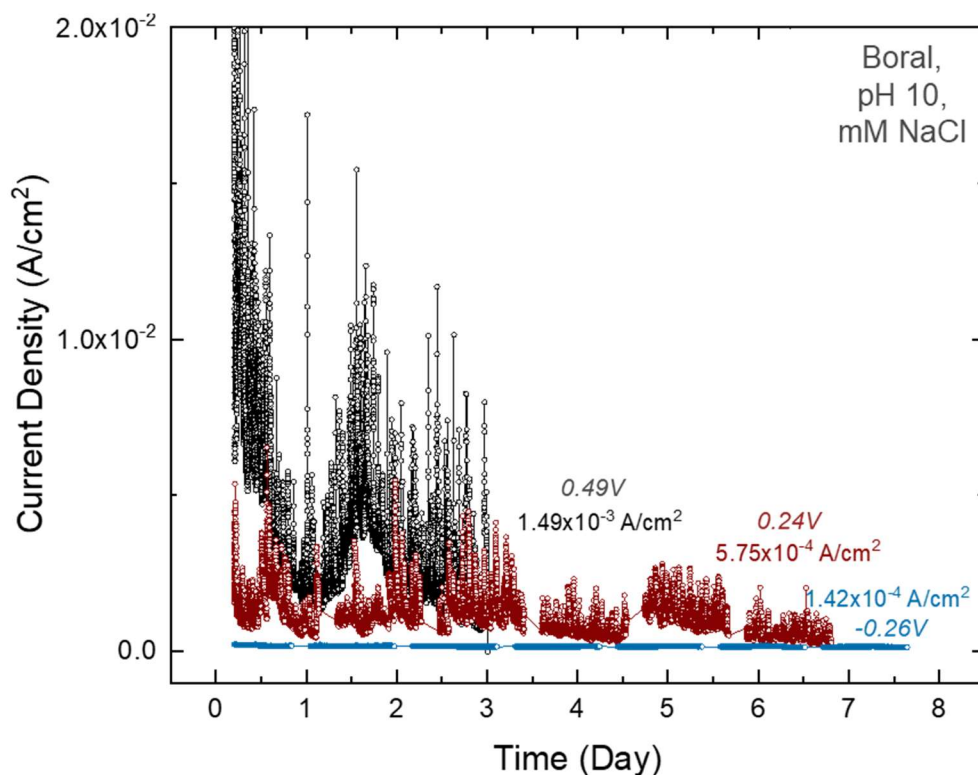


**Figure 10.** Potentiostatic test results on Boral at pH 10, 4.3 millimolar NaCl, and various fixed potentials ( $V_{SHE}$ ).

The Boral corrosion rates, which were only measured at pH 10 and in 4.3 millimolar NaCl solution, are nearly the same order of magnitude as those measured for carbon steel under the same conditions (Table 1). Corrosion of the Al cladding of the Boral material forms porous aluminum oxide/hydroxide corrosion products that do not effectively passivate the surface and high corrosion rates persist. The currents measured in the potentiostatic tests with the Boral at pH 10, 4.3 millimolar NaCl, and positive hold potentials (i.e.,  $0.49 V_{SHE}$  and  $0.24 V_{SHE}$ ) are erratic during the measurement (Figure 10), probably due to pitting. The average of the current density values beyond Day 1 was used to calculate the corrosion rate.

Figure 11 shows the corrosion rate data trends for tests with carbon steel as a function of applied potential in different electrolyte compositions. The best-fit lines in the plot depict the relationship between corrosion rate and applied potential. The increase in the carbon steel corrosion rate with increasing NaCl concentration is clear in Figure 11.

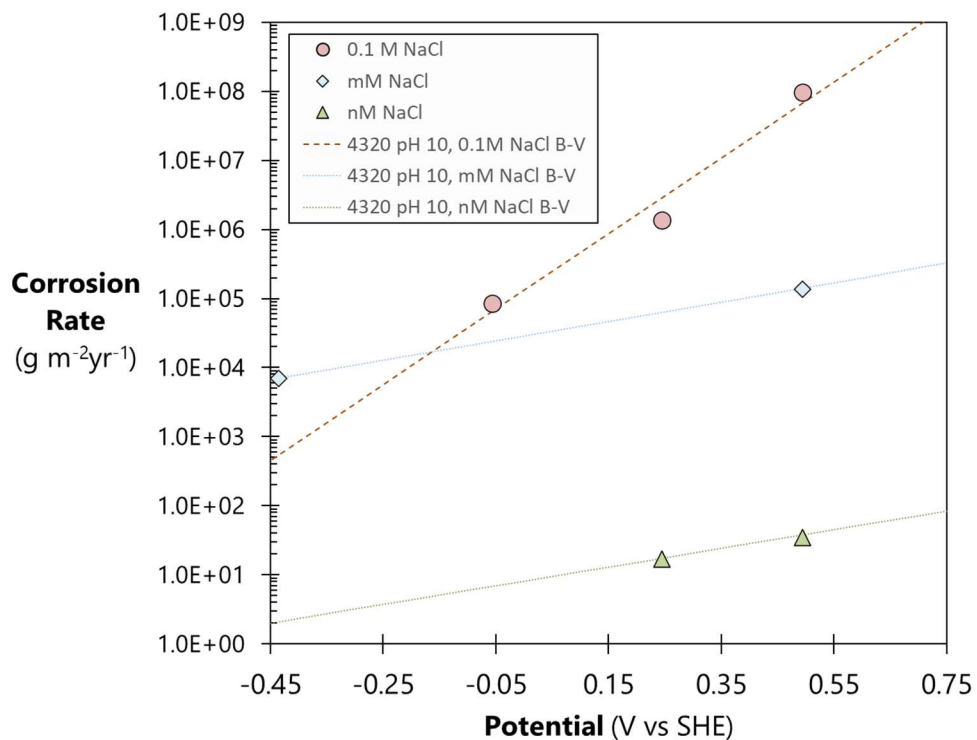


**Figure 11.** Corrosion rates plotted against potentiostatic fixed potentials ( $V_{SHE}$ ) for AISI 4320 (carbon steel) at pH 10 and various NaCl concentrations overlaid with exponential best-fit lines (Equations 6 – 8).

The best trendline fits to the data shown in Figure 11 are exponential relationships:

For the 0.1 molal data the fit is:

$$CR = 1.253 \times 10^5 \cdot \exp(12.683 \cdot E), R^2: 0.97 \quad (\text{Equation 6})$$

For the millimolal data the trend is:

$$CR = 2.81 \times 10^4 \cdot \exp(3.193 \cdot E) \quad (\text{Equation 7})$$

And for the nanomolal data the trend is:

$$CR = 8.413 \cdot \exp(2.879 \cdot E) \quad (\text{Equation 8})$$

The corrosion rates for AISI 4320 plotted as functions of pH and chloride concentrations are shown in Figures 12 and 13.

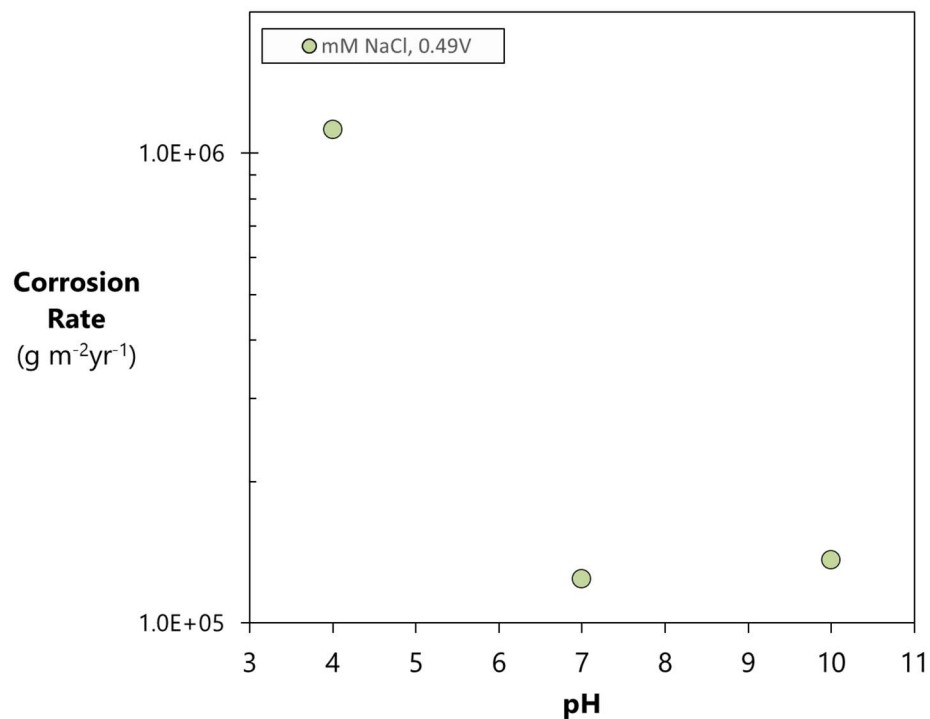


**Figure 12.** Corrosion rates plotted against pH for AISI 4320 (carbon steel) at 4.3 millimolar NaCl concentration and 0.49 V<sub>SHE</sub>.

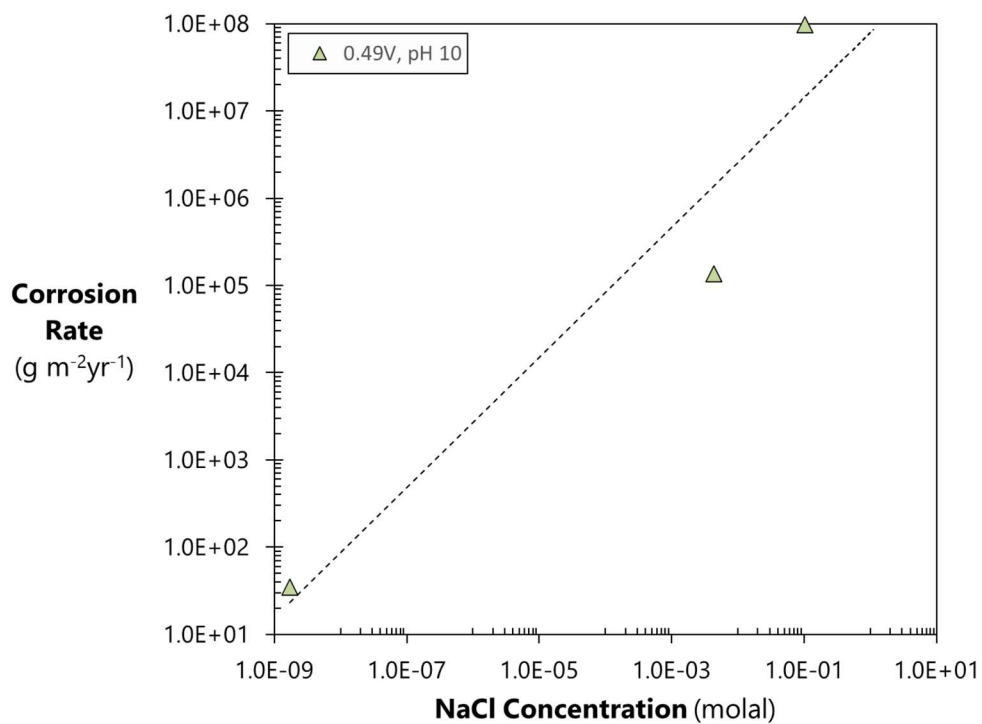


**Figure 13.** Corrosion rates plotted against pH for AISI 4320 (carbon steel) at pH 10 and 0.49 V<sub>SHE</sub> (regression line is given in Equation 9).

The NaCl concentration dependence of the carbon steel corrosion rate is fit best by a power law:

$$CR = 8.0 \times 10^7 \cdot [NaCl]^{0.7454}, R^2 = 0.918 \quad (\text{Equation 9})$$

Figure 14 shows the corrosion rate data trends as a function of applied potential in different electrolyte compositions for the borated aluminum composite material Boral. The best-fit line in the plot depicts the relationship between the corrosion rate and redox potential.

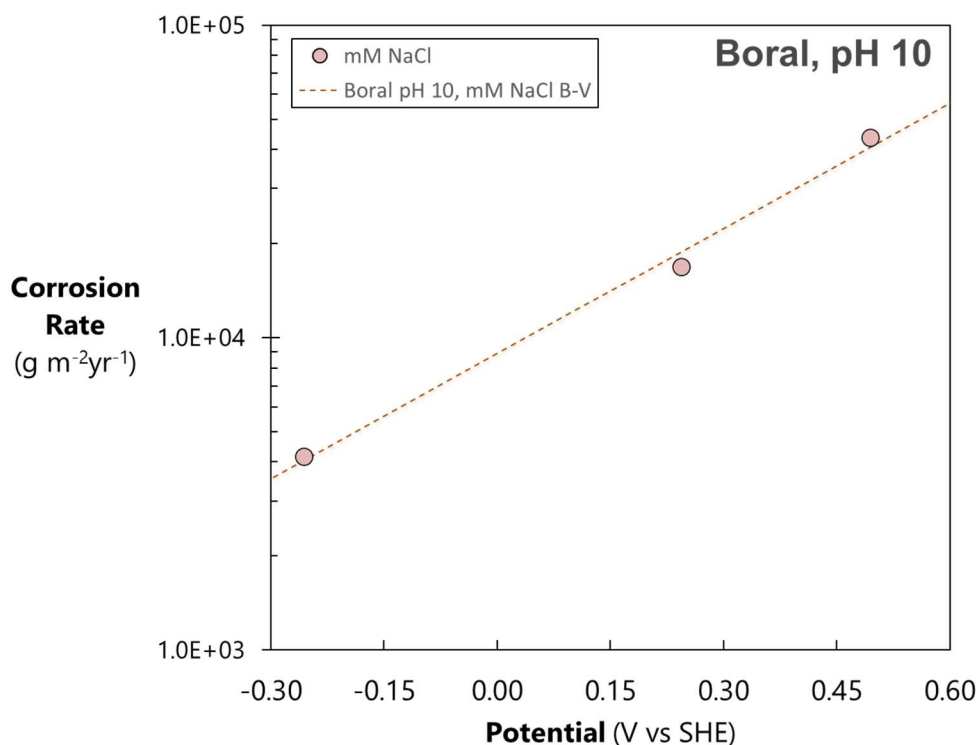


**Figure 14.** Corrosion rates plotted against potentiostatic fixed potentials ( $V_{SHE}$ ) for Boral at pH 10 and 4.3 millimolar NaCl overlaid with an exponential best-fit line (Equation 10).

The best trendline fit to the corrosion rate data for Boral shown in Figure 14 is an exponential relationship:

$$CR = 8.88 \times 10^3 \cdot \exp(3.086 \cdot E), R^2: 0.994 \quad (\text{Equation 10})$$



### 3.3.2 316 Stainless Steel

Table 2 reports the current densities and corrosion rates of 316 stainless steel measured at various pH, NaCl concentration, and hold potential. The highest corrosion rate ( $1.2 \times 10^3 \text{ g m}^{-2} \text{ yr}^{-1}$ ) was measured in the solution containing 630 millimolal NaCl at pH 4 and held at 0.49 V<sub>SHE</sub> and the lowest corrosion rate ( $1.2 \times 10^{-2} \text{ g m}^{-2} \text{ yr}^{-1}$ ) was measured in the solution containing 4.3 millimolal NaCl at pH 10 and held at 0.14 V<sub>SHE</sub>. Many corrosion tests that were run below 0.14 V<sub>SHE</sub>, and a few that were run above, showed net cathodic currents (i.e., negative values for current density), signifying that measurement potentials were lower than E<sub>corr</sub>.

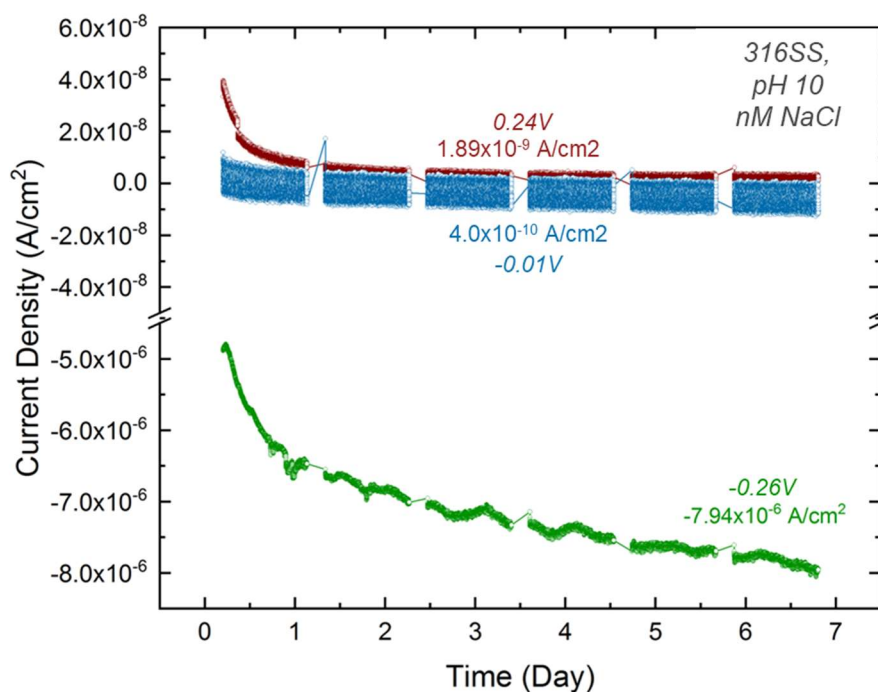
**Table 2.** Current densities and corrosion rates from electrochemical corrosion tests on 316 stainless steel

Alloy	pH	NaCl (molal)	Quantity*	Volts SHE					
				0.49	0.34	0.24	0.14	-0.01	-0.26
316SS	4	1.7E-09	CD	7.1E-09	-1.8E-09	-1.3E-09	----	----	----
			CR	2.5E-02	<i>Cathodic</i>	<i>Cathodic</i>	----	----	----
		4.3E-03	CD	8.6E-09	2.7E-09	1.2E-09	-1.1E-09	----	----
			CR	7.2E-01	2.3E-01	1.0E-01	<i>Cathodic</i>	----	----
		1.0E-01	CD	7.1E-09	2.7E-09	1.5E-09	----	----	----
			CR	5.9E-01	2.3E-01	1.2E-01	----	----	----
		6.3E-01	CD	1.4E-05	3.3E-09	----	----	----	----
			CR	1.2E+03	2.8E-01	----	----	----	----
	7	1.7E-09	CD	3.2E-09	2.5E-09	7.0E-10	----	-3.2E-06	-2.5E-09
			CR	2.7E-01	2.1E-01	5.9E-02	----	<i>Cathodic</i>	<i>Cathodic</i>
		4.3E-03	CD	4.1E-08	3.4E-09	2.6E-09	4.3E-09	-1.7E-07	-8.2E-06
			CR	3.4E+00	2.9E-01	2.1E-01	3.6E-01	<i>Cathodic</i>	<i>Cathodic</i>
		1.0E-01	CD	1.2E-08	1.6E-09	3.9E-09	----	-6.4E-08	-4.5E-06
			CR	9.6E-01	1.3E-01	3.2E-01	----	<i>Cathodic</i>	<i>Cathodic</i>
		6.3E-01	CD	1.1E-08	1.3E-08	----	----	----	----
			CR	8.8E-01	1.0E+00	----	----	----	----
	10	1.7E-09	CD	5.1E-09	2.0E-10	1.9E-09	----	4.0E-10	-7.9E-06
			CR	4.3E-01	1.6E-02	1.6E-01	----	3.4E-02	<i>Cathodic</i>
		4.3E-03	CD	3.2E-09	1.0E-09	4.9E-10	1.4E-10	-1.5E-09	-3.8E-06
			CR	2.7E-01	8.5E-02	4.1E-02	1.2E-02	<i>Cathodic</i>	<i>Cathodic</i>

		1.0E-01	CD	2.0E-09	5.1E-09	-6.7E-10	----	-8.1E-08	-8.7E-06
			CR	1.7E-01	4.2E-01	<i>Cathodic</i>	----	<i>Cathodic</i>	<i>Cathodic</i>
		6.3E-01	CD	8.2E-10	2.9E-09	----	----	----	----
			CR	6.8E-02	2.4E-01	----	----	----	----

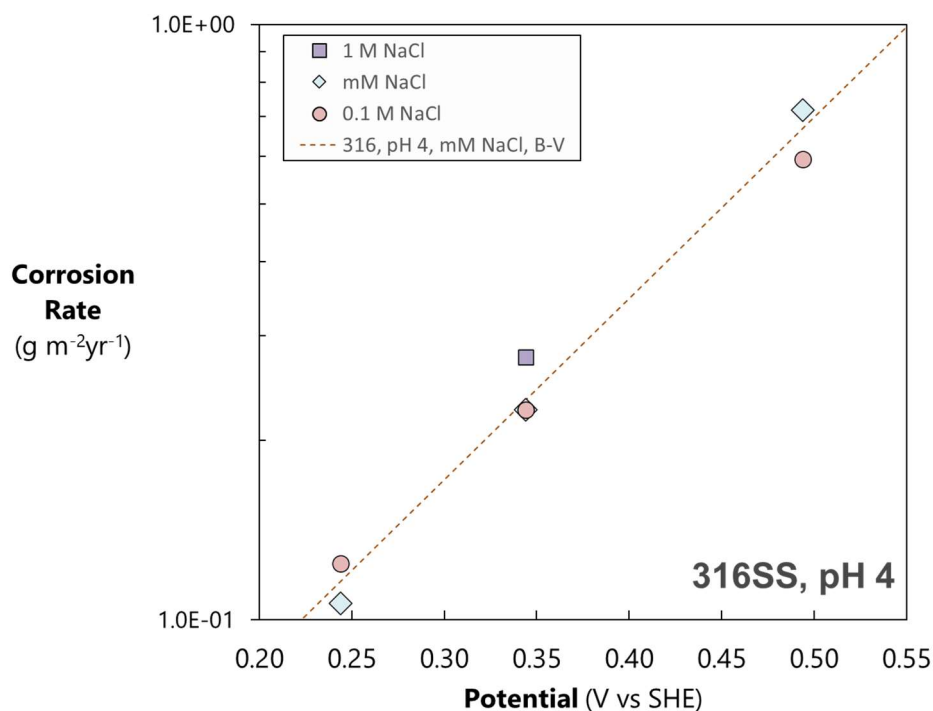
\*CD = current density ( $A\ cm^{-2}$ ), CR = Corrosion Rate ( $g\ m^{-2}yr^{-1}$ ), ---- = not measured.

Figure 15 presents representative data from potentiostatic tests on 316 stainless steel measured in solutions containing 17 nanomolal NaCl at pH 10 and at 3 designated hold potentials. The gaps in the current profiles are due to the performance of electrochemical impedance spectroscopy (EIS), the results of which will be discussed in a future report. The thickness of the curves are a result of the dynamic balance between anodic and cathodic reactions occurring of the electrode surface, and the higher values after about seven days were used to calculate corrosion rate. The corrosion currents stabilized relatively rapidly (after day 2) in tests at the higher potentials, coinciding with the passivation of the material by a thin chromium oxide layer. The surface did not passivate in the test at -0.26 V and a cathodic current occurred.



**Figure 15.** Potentiostatic test results on 316 stainless steel at pH 10, 17 nanomolal NaCl, and various fixed potentials ( $V_{SHE}$ ).

In general, the corrosion rates of 316 stainless steel do not vary significantly with NaCl concentration at pH 4 and 7, which is apparent from the overlaid datasets in Figures 16 and 17, respectively. Representative best-fit lines are shown for the data collected in solutions of 4.3 millimolal NaCl for both plots (Figures 16 and 17). At pH 10, the corrosion rate of 316 stainless steel is dependent on NaCl concentration (Figure 18). For the hold potentials measured in this study, the corrosion rates in solutions of 1.7 nanomolal NaCl are approximately an order of magnitude greater than in solutions of 4.3 millimolal NaCl. However, in solutions of 0.1 molal NaCl and 1 molal NaCl, the corrosion rate unexpectedly decreases with increasing hold potential (Figure 18).



**Figure 16.** Corrosion rates plotted against potentiostatic fixed potentials ( $V_{\text{SHE}}$ ) for 316 stainless steel at pH 4 and various NaCl concentrations overlaid with an exponential best-fit line (Equation 11).

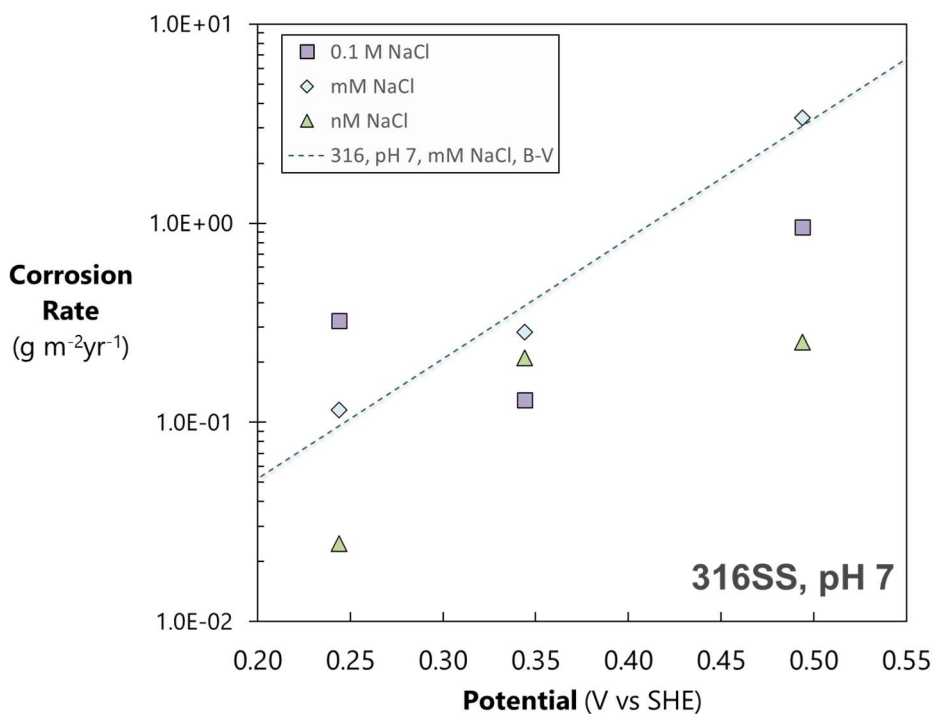


**Figure 17.** Corrosion rates plotted against potentiostatic fixed potentials ( $V_{\text{SHE}}$ ) for 316 stainless steel at pH 7 and various NaCl concentrations overlaid with an exponential best-fit line.

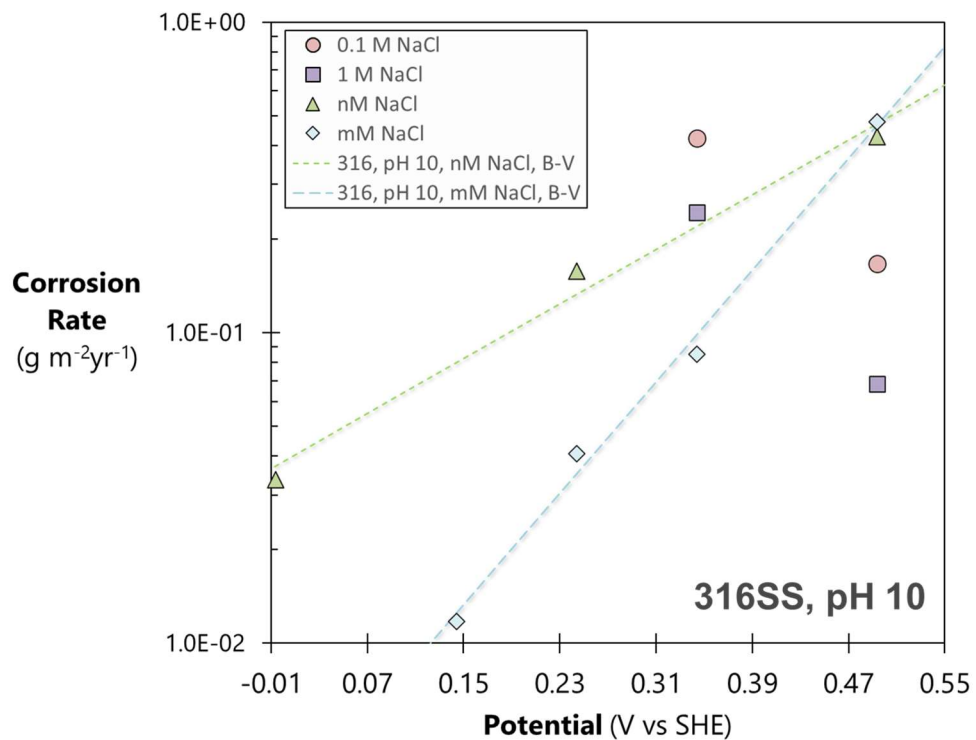


**Figure 18.** Corrosion rates plotted against potentiostatic fixed potentials ( $V_{SHE}$ ) for 316 stainless steel at pH 10 and various NaCl concentrations overlaid with exponential best-fit lines (Equations 13 and 14).

The best fit trendlines for the corrosion rate data shown in Figures 16, 17 and 18 are exponential relationships:

for the stainless steel corrosion at pH 4 (Figure 16) the relationship for the 4.3 millimolal data is:

$$CR = 1.64 \times 10^{-2} \cdot \exp(7.638 \cdot E), R^2: 0.999 \quad (\text{Equation 11})$$

the relationship at pH 7 (Figure 17) for the 4.3 millimolal data is:

$$CR = 3.4 \times 10^{-3} \cdot \exp(13.734 \cdot E), R^2: 0.978 \quad (\text{Equation 12})$$

the relationship at pH 10 (Figure 18) for the 4.3 millimolal data is:

$$CR = 2.8 \times 10^{-3} \cdot \exp(10.33 \cdot E), R^2: 0.993 \quad (\text{Equation 13})$$

and the best fit trend for the nanomolal data shown in Figure 18 is:

$$CR = 3.8 \times 10^{-2} \cdot \exp(5.079 \cdot E), R^2: 0.985 \quad (\text{Equation 14})$$

The pH dependence of the 316 stainless steel corrosion rates are shown in Figures 19, 20 and 21.

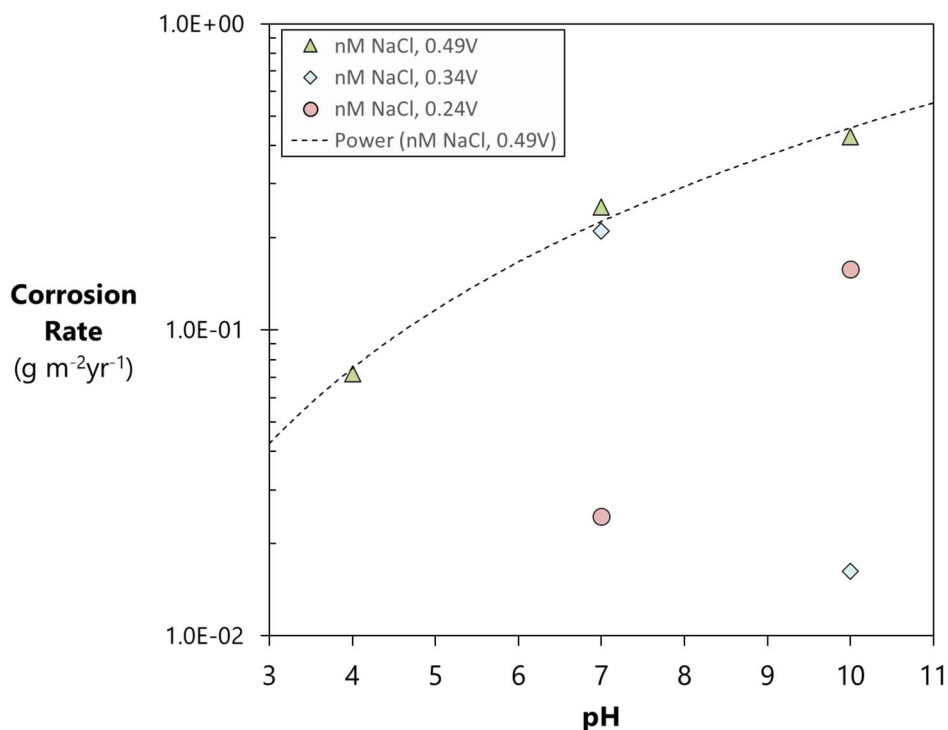


**Figure 19.** Corrosion rates plotted against pH for 316 stainless steel at 1.7 nanomolal NaCl concentration.

The best fit trend line for the pH dependence of the stainless steel corrosion rate at 0.49 V shown in Figure 19 is a power law function:

$$CR = 0.0049 \cdot [pH]^{1.974}, R^2 = 0.989 \quad (\text{Equation 15})$$

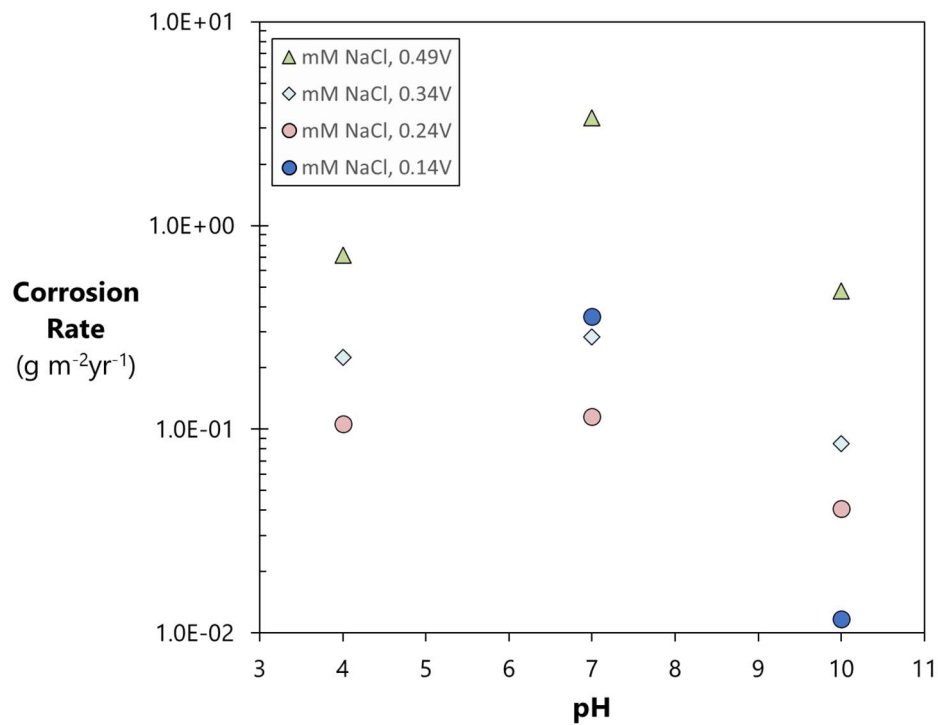


**Figure 19.** Corrosion rates plotted against pH for 316 stainless steel at 4.3 nanomolar NaCl concentration.

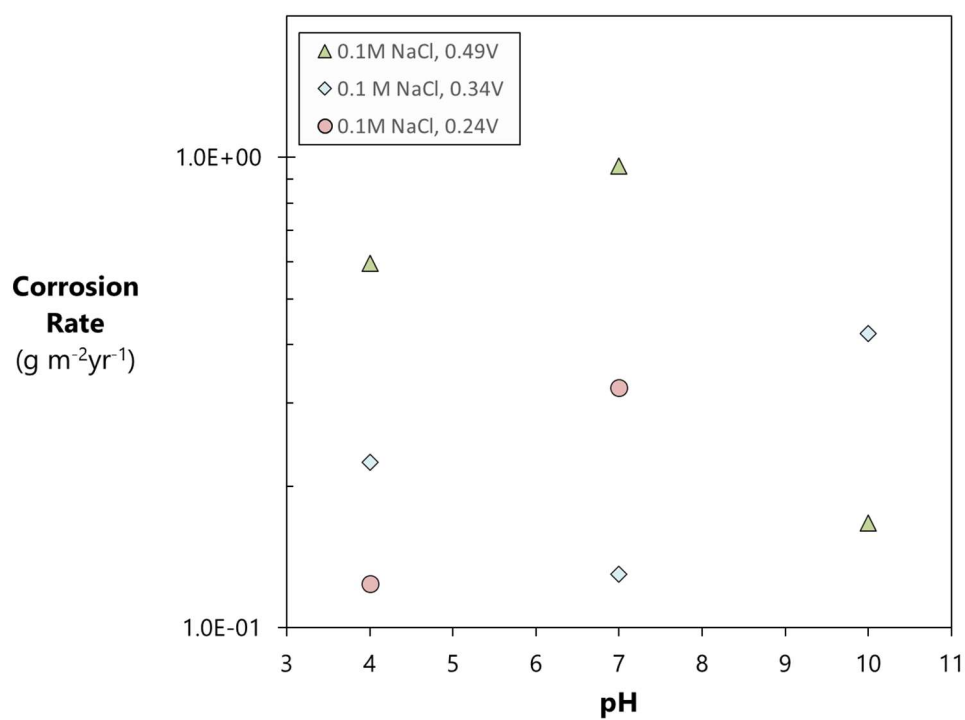


**Figure 20.** Corrosion rates plotted against pH for 316 stainless steel at 0.1 molal NaCl concentration.

The data shown in Figures 20 and 21 do not show regular trends for the stainless steel corrosion rate dependence on pH.

The dependence of the stainless steel corrosion rate on salt concentration are shown in Figures 22, 23 and 24. These data generally do not show regular trends.

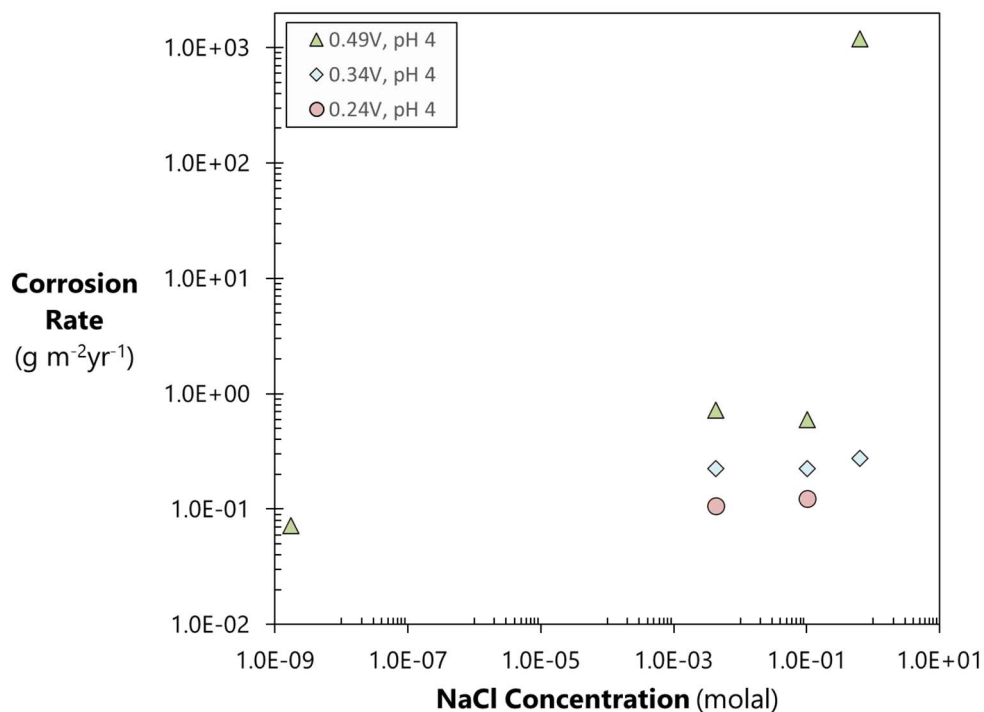


**Figure 21.** Corrosion rates plotted as a function of NaCl concentration 316 stainless steel at pH 4.

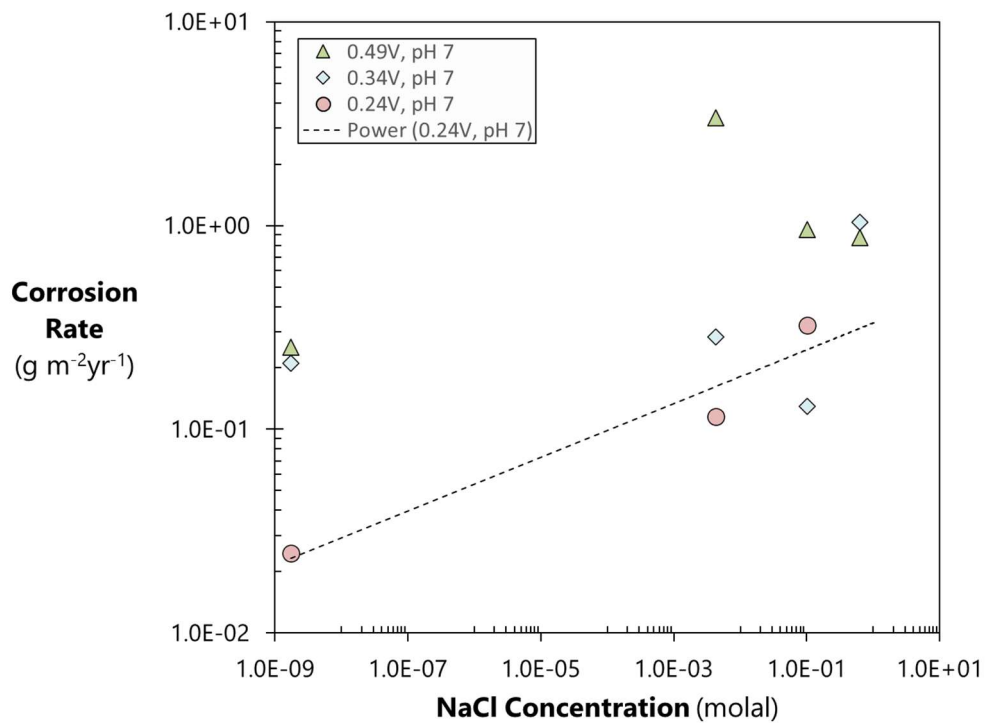


**Figure 22.** Corrosion rates plotted as a function of NaCl concentration 316 stainless steel at pH 7.

The stainless steel corrosion rate dependence on the NaCl concentrations for the 0.24 V data shown in Figure 23 is best fit by a power law:

$$CR = 0.3326 \cdot [\text{NaCl}]^{0.132}, R^2: 0.943 \quad (\text{Equation 16})$$



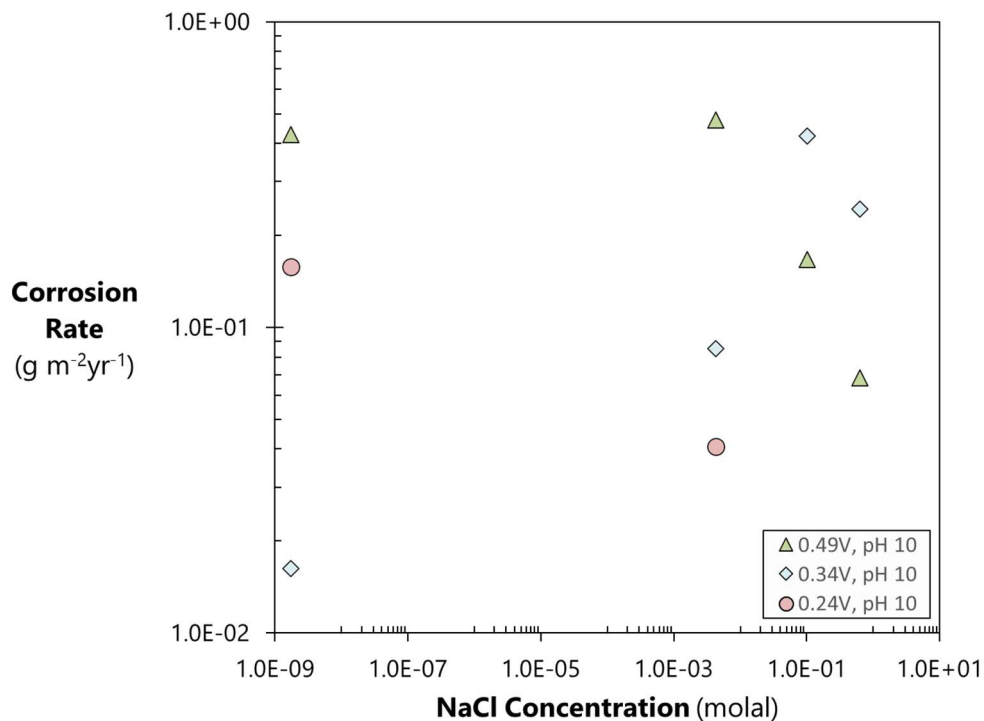


**Figure 23.** Corrosion rates plotted as a function of NaCl concentration 316 stainless steel at pH 10.

### 3.3.3 Zircaloy-4

The corrosion test results for Zircaloy-4 are provided in Table 3. The highest measured corrosion rate ( $6.1 \times 10^{-1} \text{ g m}^{-2} \text{ yr}^{-1}$ ) is reported at pH 10, 100 millimolal NaCl, and  $0.49 \text{ V}_{\text{SHE}}$ , and the lowest measured corrosion rate, which is just an order of magnitude lower ( $5.4 \times 10^{-2} \text{ g m}^{-2} \text{ yr}^{-1}$ ), is reported at pH 10, 4.3 millimolal NaCl, and  $-0.01 \text{ V}_{\text{SHE}}$ .

**Table 3.** Current densities and corrosion rates from electrochemical corrosion tests on Zircaloy-4

Alloy	pH	NaCl (molal)	Quantity*	Volts SHE				
				<i>0.49</i>	<i>0.34</i>	<i>0.24</i>	<i>-0.01</i>	<i>-0.46</i>
Zircaloy-4	4	1.7E-09	CD	1.1E-09	----	----	----	----
			CR	8.0E-02	----	----	----	----
		4.3E-03	CD	3.7E-09	2.7E-09	----	----	----
			CR	2.7E-01	2.0E-01	----	----	----
		1.0E-01	CD	4.6E-09	----	----	----	----
			CR	3.4E-01	----	----	----	----
	7	1.7E-09	CD	2.9E-09	----	----	----	----
			CR	2.2E-01	----	----	----	----
		4.3E-03	CD	2.5E-09	----	----	----	----
			CR	1.9E-01	----	----	----	----
		1.0E-01	CD	4.8E-09	----	----	----	----
			CR	3.6E-01	----	----	----	----
	10	1.7E-09	CD	2.6E-09	----	1.7E-09	----	----
			CR	1.9E-01	----	1.3E-01	----	----
		4.3E-03	CD	5.6E-09	----	2.5E-09	7.3E-10	-2.6E-07
			CR	4.2E-01	----	1.8E-01	5.4E-02	Cathodic
		1.0E-01	CD	8.2E-09	----	1.7E-09	1.4E-09	-4.0E-06
			CR	6.1E-01	----	1.3E-01	1.1E-01	Cathodic

\*CD = current density ( $A\ cm^{-2}$ ), CR = Corrosion Rate ( $g\ m^{-2}yr^{-1}$ ), ---- = not measured.

Figure 25 depicts typical results from potentiostatic tests on Zircaloy-4. Steady state is reached relatively rapidly (by day 3) with very low current densities, which is due to the formation of a zirconium oxide layer that protects the surface from corrosion by limiting the diffusion of reactive chemical species. The corrosion rates of Zircaloy-4 are minimally affected by the NaCl concentration in solution, which is shown for tests at pH 10 in Figure 26. The dotted line in Figure 26 is the best-fit line for the data collected in solutions of 4.3 mM NaCl.

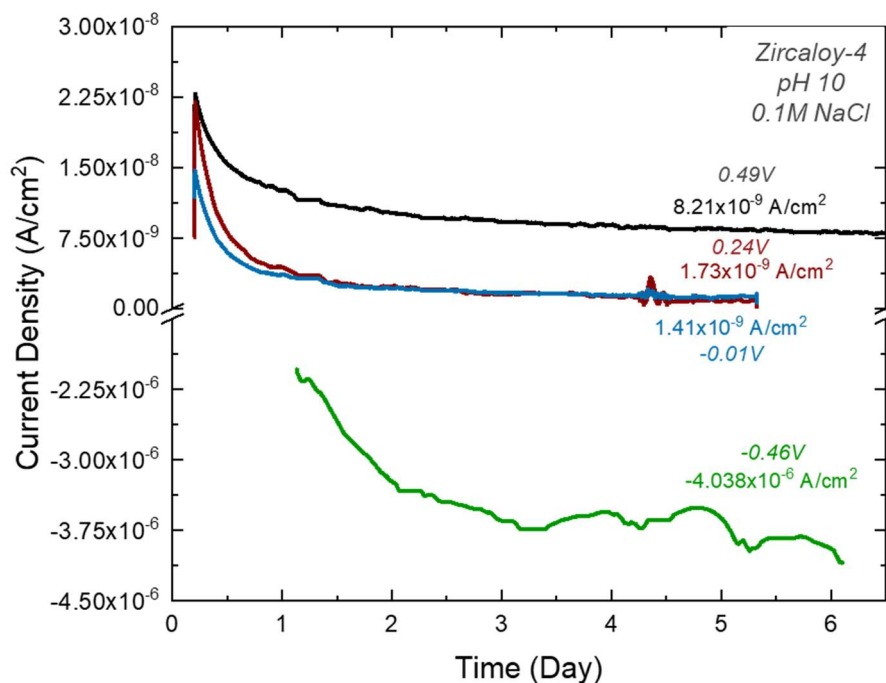


**Figure 24.** Potentiostatic test results on Zircaloy-4 at pH 10, 0.1 molal NaCl, and various fixed potentials ( $V_{\text{SHE}}$ ).

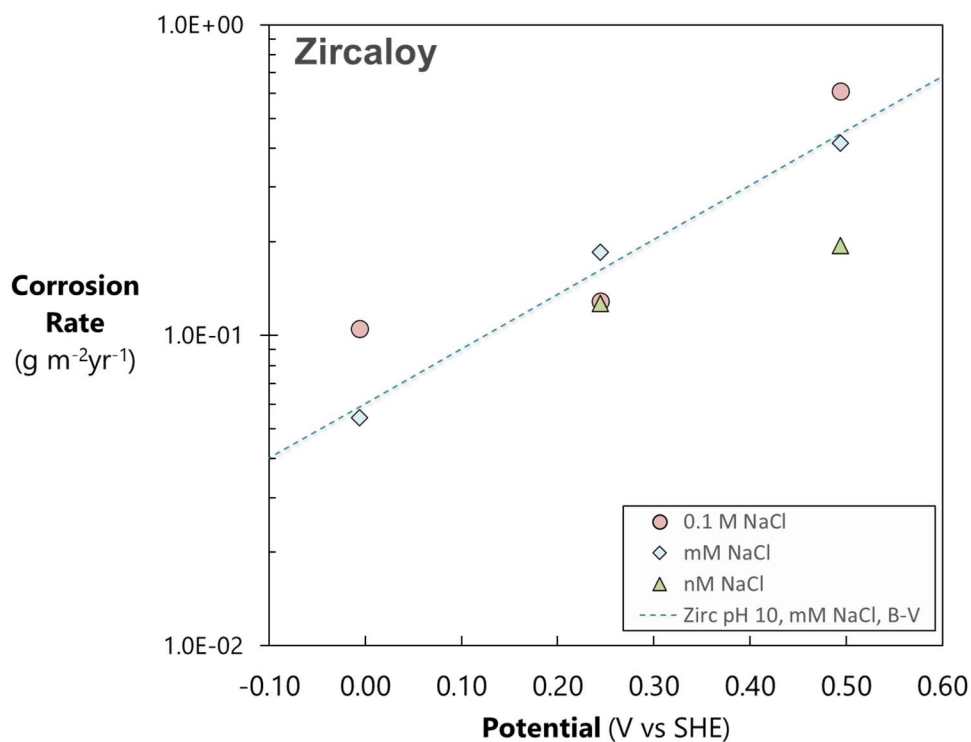


**Figure 25.** Corrosion rates plotted against potentiostatic fixed potentials ( $V_{\text{SHE}}$ ) for Zircaloy-4 at pH 10 and various NaCl concentrations overlaid with an exponential best-fit line (Equation 17).

The dependence of the Zircaloy corrosion rate on potential is best fit by an exponential relationship. The best fit trend line for the 4.3 millimolar data in Figure 26 is:

$$CR = 5.97 \times 10^{-2} \cdot \exp(4.074 \cdot E), R^2: 0.987 \quad (\text{Equation 17})$$

The dependence of the Zircaloy corrosion rate on pH is shown in Figure 27. The trend lines shown in the plot are, for the 0.1 molal data:

$$CR = 0.138 \cdot [\text{pH}]^{0.5939}, R^2: 0.72 \quad (\text{Equation 18})$$

And for the nanomolar data:

$$CR = 0.021 \cdot [\text{pH}]^{1.045}, R^2: 0.78 \quad (\text{Equation 19})$$

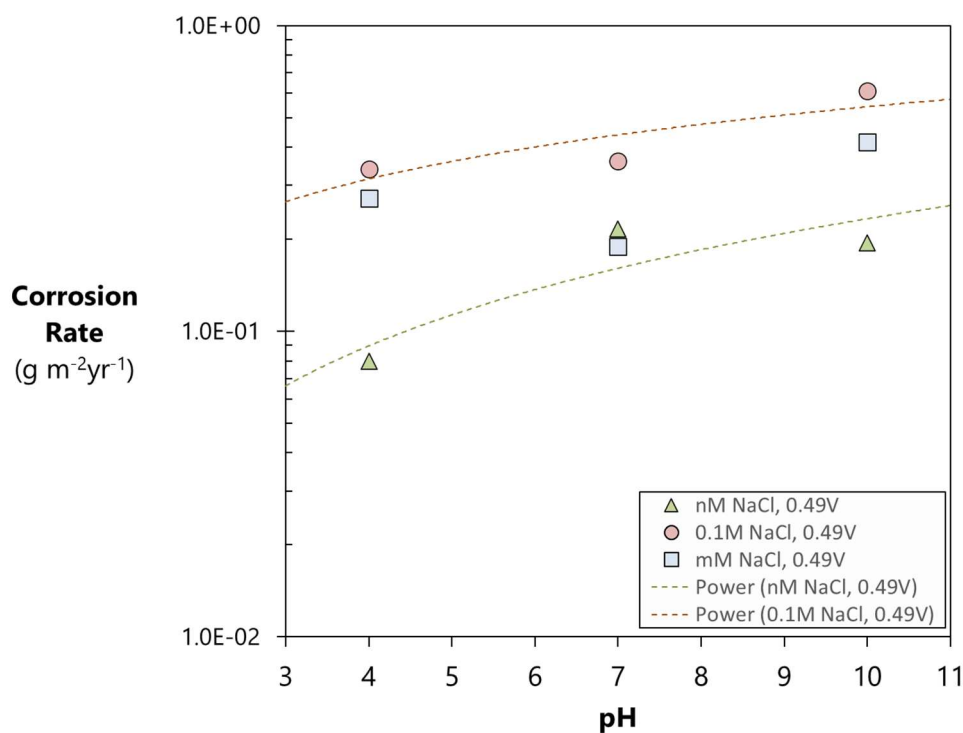


**Figure 26.** Corrosion rates plotted against pH for Zircaloy at 0.49 V<sub>SHE</sub>. The trendlines shown are defined in Equations 18 and 19.

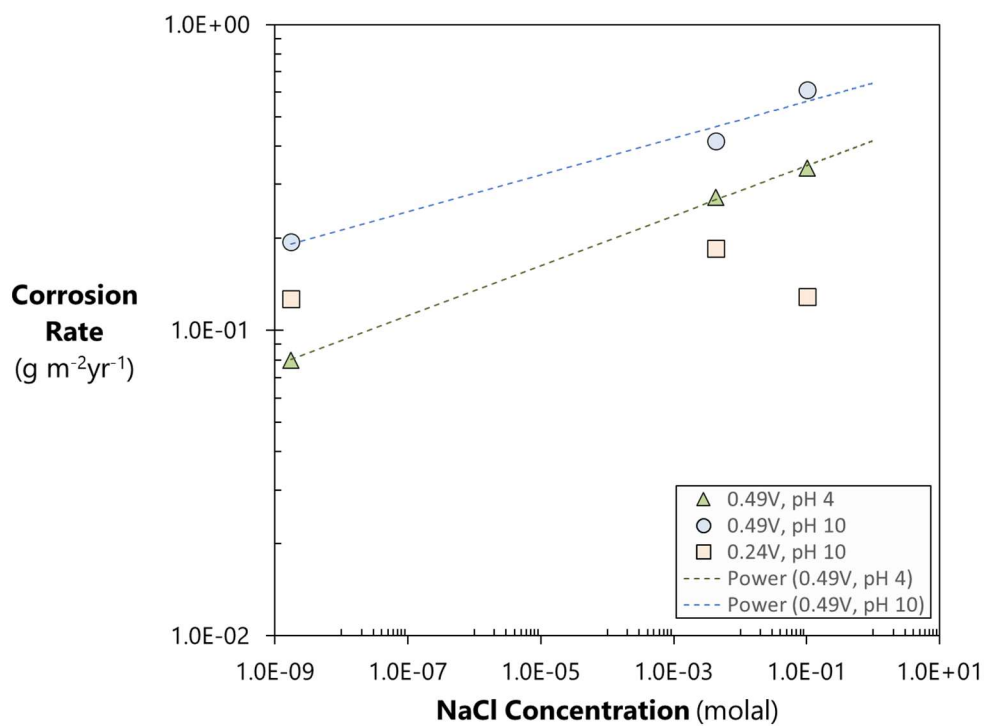


**Figure 27.** Zircaloy corrosion rates plotted as a function of NaCl concentration. The trendlines are defined in Equations 20 and 21.

The dependence of the Zircaloy corrosion rates on the chloride concentration (Figure 28) are best fit by the following power laws for the 0.49 V, pH 10 and 0.49 V, pH 10 data respectively:

$$CR = 0.644 \cdot [\text{NaCl}]^{0.0602}, R^2: 0.972 \quad (\text{Equation 20})$$

$$CR = 0.417 \cdot [\text{NaCl}]^{0.0817}, R^2: 0.999 \quad (\text{Equation 21})$$

### 3.4 Summary of Electrochemical Corrosion Tests

Figures 29 and 30 show the best fit trends for all of the electrochemical experiments described above. The dotted lines indicate the corrosion rates used for the IPC – FMD model sensitivity model runs discussed in Section 4.0 below. By comparing Figures 29 and 30, it is clear that, on average, carbon steel and Boral exhibit corrosion rates that are orders of magnitude higher than 316 stainless steel and Zircaloy-4. In addition, the corrosion rate of carbon steel at millimolar concentrations of NaCl is much greater than at nanomolar concentrations of NaCl. During electrochemical corrosion tests, a passivating layer that is effective at protecting the surface from corrosion does not build up on the carbon steel and Boral surface, which explains the high corrosion rates measured in this study. In contrast, effective metal oxide/hydroxide passivating layers do build up relatively quickly on 316 stainless steel and Zircaloy-4 surfaces, accounting for the low corrosion rates measured for these materials.

It should be noted that the relationships represented in Figures 29 and 30 were extrapolated based on the data sets shown in Figures 9 to 28 above. Future measurements will further quantify the alloy corrosion rate dependence on pH, chloride concentrations and temperature to produce more accurate and applicable analytical functions. The empirical relationships that describe the datasets shown in Figures 9 – 28 are shown in Table 4.

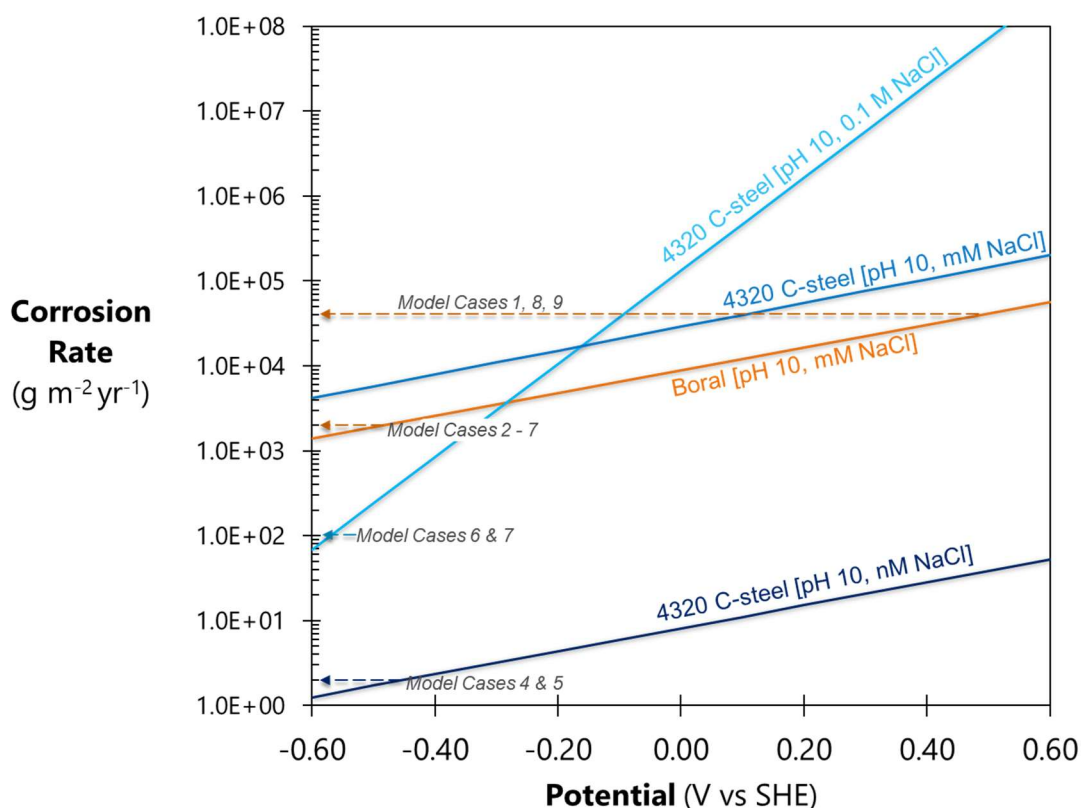


**Figure 29.** Comparisons of corrosion rate vs. potential ( $V_{SHE}$ ) for AISI 4320 (carbon steel) and Boral at pH 10 and a range of NaCl concentrations. The dotted lines indicate the corrosion rates used in the IPC – FMD model sensitivity runs discussed in Section 4 below.

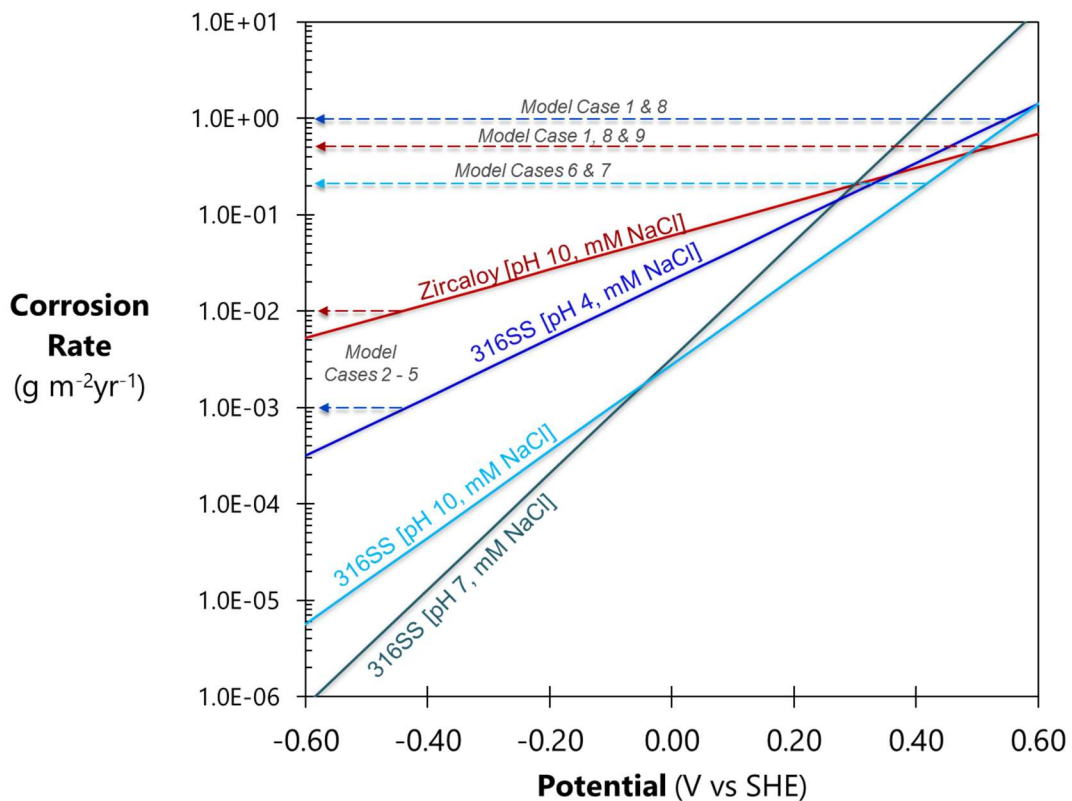


**Figure 28.** Comparisons of corrosion rate vs. potential ( $V_{SHE}$ ) for 316 stainless steel and Zircaloy-4 at mM NaCl and a range of fixed pH values. The dotted lines indicate the corrosion rates used in the IPC – FMD model sensitivity runs discussed in Section 4 below.

**Table 4.** Empirical functions (Equations 6 – 21) derived from the potentiostatic test results discussed in Section 3.3.

Alloy	Test Conditions	Empirical Function*	R <sup>2</sup>
AISI 4320 (C-steel)	0.1 M NaCl, pH 10	$CR = 1.253 \times 10^5 \cdot \exp(12.683 \cdot E)$	0.97
AISI 4320 (C-steel)	4.3 mM NaCl, pH 10	$CR = 2.81 \times 10^4 \cdot \exp(3.193 \cdot E)$	2 points
AISI 4320 (C-steel)	1.7 nM NaCl, pH 10	$CR = 8.413 \cdot \exp(2.879 \cdot E)$	2 points
Boral	4.3 mM NaCl, pH 10	$CR = 8.88 \times 10^3 \cdot \exp(3.086 \cdot E)$	0.994
316SS	4.3 mM NaCl, pH 4	$CR = 1.64 \times 10^{-2} \cdot \exp(7.638 \cdot E)$	0.999
316SS	4.3 mM NaCl, pH 7	$CR = 3.4 \times 10^{-3} \cdot \exp(13.734 \cdot E)$	0.978
316SS	4.3 mM NaCl, pH 10	$CR = 2.8 \times 10^{-3} \cdot \exp(10.33 \cdot E)$	0.993
316SS	1.7 nM NaCl, pH 10	$CR = 3.8 \times 10^{-2} \cdot \exp(5.079 \cdot E)$	0.985
Zircaloy-4	4.3 mM NaCl, pH 10	$CR = 5.97 \times 10^{-2} \cdot \exp(4.074 \cdot E)$	0.987
316SS	0.49 V <sub>SHE</sub> , 1.7 nM NaCl	$CR = 0.0049 \cdot [\text{pH}]^{1.974}$	0.989
Zircaloy-4	0.49 V <sub>SHE</sub> , 0.1 M NaCl	$CR = 0.138 \cdot [\text{pH}]^{0.5939}$	0.72
Zircaloy-4	0.49 V <sub>SHE</sub> , 1.7 nM NaCl	$CR = 0.021 \cdot [\text{pH}]^{1.045}$	0.78
AISI 4320 (C-steel)	0.49 V <sub>SHE</sub> , pH 10	$CR = 8.0 \times 10^7 \cdot [\text{NaCl}]^{0.7454}$	0.918
316SS	0.24 V <sub>SHE</sub> , pH 7	$CR = 0.3326 \cdot [\text{NaCl}]^{0.132}$	0.943
Zircaloy-4	0.49 V <sub>SHE</sub> , pH 10	$CR = 0.644 \cdot [\text{NaCl}]^{0.0602}$	0.972
Zircaloy-4	0.24 V <sub>SHE</sub> , pH 4	$CR = 0.417 \cdot [\text{NaCl}]^{0.0817}$	0.999

\*CR: corrosion rate, E: the applied potential for the potentiostatic tests (represents Eh).



#### 4. IN-PACKAGE CHEMISTRY SIMULATION AND THE FUEL MATRIX DEGRADATION MODEL: ROLE OF ALLOY CORROSION

Building on the modeling approach described in Jerden et al., 2019, the 1-D reactive transport code X1t (a module within the Geochemist's Workbench (GWB) software package) was used to implement a prototype in-package chemistry (IPC) model that was coupled to the FMD model. The IPC model was used to track how the corrosion rates of in-package alloy components and the resulting  $H_2$  concentrations evolve over a range of repository relevant time scales and conditions. The coupled FMD model determines how the spent fuel degradation rate changes based on  $H_2$  concentration history calculated by the X1t IPC model. The models were parameterized using the experimental data discussed in Section 3 above.

The thermodynamic database used for this model was thermo.com.V8.R6 (Johnson et al, 2000) to which the steel reactants were added. The masses of the different steel components, their surface areas, and total solution volume were those given in the in-package chemistry model used for the YM TSPA (CRWMS, 2003). The alloy masses used for this model are shown in Table 5, and the initial groundwater composition, which is typical of an argillite rock repository environment, is shown in Table 6. The volume of solution used in the model was  $4.1 \text{ m}^3$ , which is based on the void volume within the spent fuel canister assumed in CRWMS, 2003.

**Table 5.** Alloy masses and specific surface areas used in the X1t in-package chemistry model (values are from CRWMS, 2003)

Materials	Total Mass (kg)	Specific Surface Area ( $\text{m}^2 \text{ g}^{-1}$ )
316 SS	$5.9 \times 10^3$	$4.1 \times 10^{-6}$
C-steel	$1.2 \times 10^3$	$8.7 \times 10^{-5}$
Aluminum alloy*	$1.9 \times 10^2$	$2.8 \times 10^{-4}$
Zircaloy cladding	$3.6 \times 10^2$	$1.3 \times 10^{-3}$
Spent Fuel	$2.9 \times 10^4$	$1.6 \times 10^{-5}$

\*Indicated as "Boral" in discussion and figures below.

**Table 6.** Initial solution composition used in X1t in-package chemistry model (from Fernandez et al., 2007). This composition is typical pore-water from the Opalinus clay.

Component	Concentration (molar)
pH	7.4
Na	$2.8 \times 10^{-1}$
Ca	$2.3 \times 10^{-2}$
K	$2.2 \times 10^{-3}$
Mg	$2.1 \times 10^{-2}$
Fe	$3.5 \times 10^{-6}$
$\text{Cl}^-$	$3.3 \times 10^{-1}$
$\text{SO}_4^{2-}$	$1.9 \times 10^{-2}$
$\text{CO}_3^{3-}$	$5.2 \times 10^{-3}$
$\text{SiO}_2$	$1.1 \times 10^{-4}$

Figure 31 shows the flow of information for the coupled X1t – FMD model as well as the schematic layout and discretization of X1t IPC model. The alloy corrosion rates discussed in Section 3 above are used to parameterize the IPC model, which tracks in package the  $H_2$  concentration based on its generation by alloy corrosion and its loss by diffusion/advection into the surroundings over the 100,000-year model time frame. The  $H_2$  concentration evolution determines the spent fuel degradation rate as calculated by the FMD model.

The X1t model includes 21 reaction/diffusion cells (not shown in Figure 31) with the central cell including the materials shown in Table 2. The diffusion coefficient used for  $H_2$  in all model cases was  $6.0 \times 10^{-5} \text{ cm}^2/\text{s}$  (Turnbull, 2008). The porosity of the waste package cell was set to 80%, while the porosity in the bentonite and host rock cells were set to 30%.

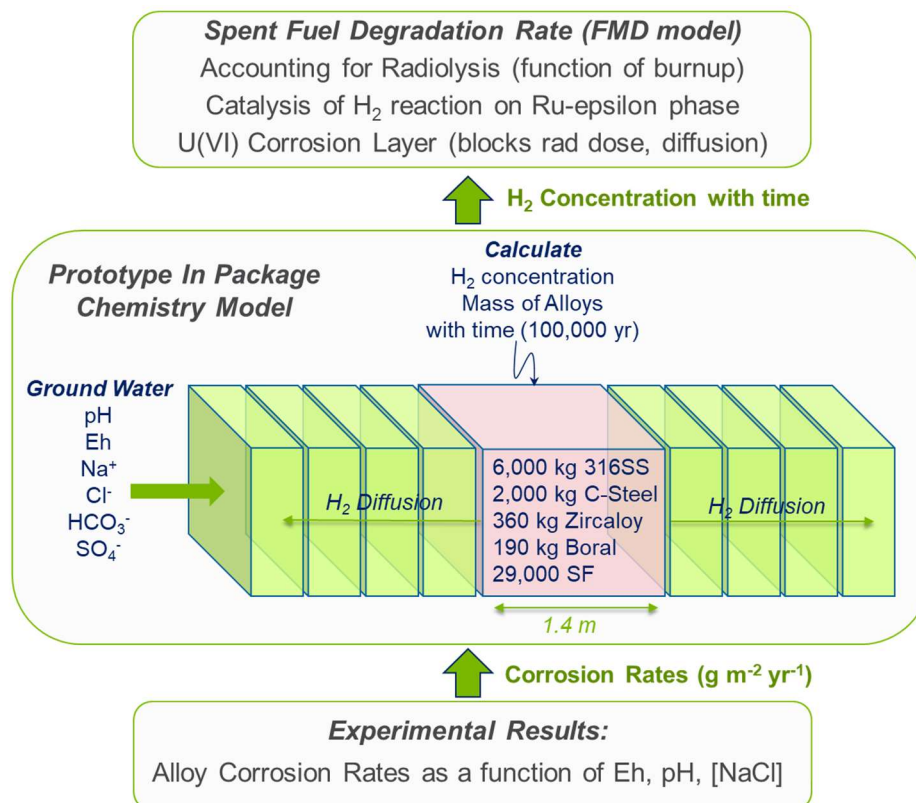


**Figure 29.** Flow of information for the coupled X1t prototype in-package chemistry and the FMD model.

Thus, the four main functions of the X1t IPC mode are to:

- Determine the amount of  $H_2$  produced and accumulated over a range of relevant alloy corrosion rates.
- Quantify the kinetics of  $H_2$  removal (by diffusion or advection) from the waste package cell containing the spent fuel.
- Track the dissolved  $H_2$  concentration within the in-package solution based on the first two bullets.
- Provide the  $H_2$  concentration as a function of time to the FMD model so that the spent fuel degradation rate can be calculated as the in-package environment evolves.

As discussed in Sections 1 and 2 above, the most significant processes accounted for in the FMD model include burnup dependent radiolysis, U(VI) corrosion layer formation and the catalytic oxidation of  $H_2$  on the noble metal alloy. The  $H_2$  oxidation process proves to be dominant, inhibiting oxidative dissolution of the fuel, when the  $H_2$  concentration is greater than a certain threshold value as discussed in Jerden et al., 2019 and shown schematically in Figure 3 above. Results from FMD modeling (discussed below) show that the  $H_2$  concentration threshold needed to shut down oxidative dissolution of the fuel depend on the burnup of the fuel. Higher burnup fuels produced more radiolytic oxidants per time and thus the amount of  $H_2$  needed to overcome the radiolytic oxidative effect is higher. Therefore, sensitivity model runs were conducted using a higher fuel burn up value of 80 GWd/MTU and a relatively low burn up value of 30 GWd/MTU. Other variables investigated in the model sensitivity runs for this study include: steel corrosion rates for different conditions (Eh, pH, NaCl concentration) and the advective rate of solution within the waste package (Table 7).

It should be noted that the X1t IPC model represents a prototype or scoping model intended to inform future development of a more versatile in-package model that will be integrated within the GDSA framework and implemented in PFLOTRAN. There are several simplifying assumptions that the model currently uses that need to be replaced by more rigorous formulations in the future. The major simplifying assumptions are for the X1t IPC model are:

- The use of first order alloy corrosion rate expressions (parameterized using data described in Section 3) that do not account for the evolving surface area of the corroding alloy.
- The neglect of galvanic effects caused by alloys being in contact within the waste package.

The results of the X1t IPC model are thus preliminary and not meant to accurately represent actual repository scenarios. Rather, the results are meant to yield insights as to how changes in in-package alloy corrosion rates influence the spent fuel degradation rate over repository relevant conditions and time scales. To this end a set of sensitivity studies were run using the range of measured alloy corrosion rates presented in Section 3 above. Table 7 shows the conditions used for the sensitivity runs and Figures 32 to 37 show the modeling results. The solution Eh, pH and [NaCl] referred to in Table 7 are the conditions for the solution flowing into the waste package during corrosion. These variables can evolve with time depending on the balance between the rate of advection/diffusion of solute into the waste package and the rates of alloy corrosion. The specific surface areas used for the alloys for each model run are shown in Table 5 above. The corrosion rates chosen for each set of Eh, pH and NaCl concentration conditions are based on the empirical relationships shown in Figures 29 and 30 above.

**Table 7.** Conditions for sensitivity runs performed using the linked X1t IPC and FMD models. The corrosion rates chosen for these model runs span the range of rates measured in the electrochemical tests discussed in Section 3 above.

Model Case	Solution Eh <sup>1</sup>	pH <sup>2</sup>	[NaCl] <sup>3</sup>	C-Steel (g m <sup>-2</sup> yr <sup>-1</sup> )	316 SS (g m <sup>-2</sup> yr <sup>-1</sup> )	Boral <sup>4</sup> (g m <sup>-2</sup> yr <sup>-1</sup> )	Zircaloy (g m <sup>-2</sup> yr <sup>-1</sup> )	Advection <sup>5</sup> (m/yr)
1	High	Low	High	1.0x10 <sup>6</sup>	1.0x10 <sup>0</sup>	4.0x10 <sup>4</sup>	5.0x10 <sup>-1</sup>	0 (diffusion only)
2	Low	Low	Low	1.0x10 <sup>6</sup>	1.0x10 <sup>-3</sup>	4.0x10 <sup>3</sup>	1.0x10 <sup>-2</sup>	0 (diffusion only)
3	Low	Low	Low	1.0x10 <sup>6</sup>	1.0x10 <sup>-3</sup>	4.0x10 <sup>3</sup>	1.0x10 <sup>-2</sup>	0.1
4	Low	High	Low	2.0x10 <sup>1</sup>	1.0x10 <sup>-3</sup>	4.0x10 <sup>3</sup>	1.0x10 <sup>-2</sup>	0 (diffusion only)
5	Low	High	Low	2.0x10 <sup>1</sup>	1.0x10 <sup>-3</sup>	4.0x10 <sup>3</sup>	1.0x10 <sup>-2</sup>	0.1
6	Low	High	High	1.0x10 <sup>2</sup>	2.0x10 <sup>-1</sup>	4.0x10 <sup>3</sup>	1.0x10 <sup>-2</sup>	0 (diffusion only)
7	Low	High	High	1.0x10 <sup>2</sup>	2.0x10 <sup>-1</sup>	4.0x10 <sup>3</sup>	1.0x10 <sup>-2</sup>	0.1
8	High	Low	Low	1.0x10 <sup>6</sup>	1.0x10 <sup>0</sup>	4.0x10 <sup>4</sup>	5.0x10 <sup>-1</sup>	0 (diffusion only)
9	High	Low	High	1.0x10 <sup>6</sup>	1.0x10 <sup>3</sup>	4.0x10 <sup>4</sup>	5.0x10 <sup>-1</sup>	0 (diffusion only)

<sup>1</sup> Low Eh denotes -0.6 V to -0.2 V (vs SHE) and high Eh denotes 0.2 V to 0.6 V (vs SHE).

<sup>2</sup> Low pH denotes a value of 4 and high pH refers value of 10 (as used in the experiments described above).

<sup>3</sup> Low [NaCl] denotes concentrations ranging from nanomolar to micromolar and high [NaCl] denotes concentrations ranging from 0.1 to 1 molal NaCl.

<sup>4</sup> Boral is a borated aluminum alloy commonly used as a neutron absorber in spent fuel storage canisters.

<sup>5</sup> Advection refers to the rate of groundwater discharge through the breached waste package.

Most of the corrosion rates used for the model runs are indicated on Figures 29 and 30 above. The corrosion rate for C-steel (AISI 4320) for the low pH model runs (Cases 1, 2, 3, 8 and 9) was 1.0x10<sup>6</sup> g m<sup>-2</sup> yr<sup>-1</sup> (row 2, Table 1) and the high corrosion rate for 316SS used in model Case 9 is from high salt concentration, low pH data shown in row 8 of Table 2.

Each model run involved the following steps:

- The initial condition of the reactive transport domain (Figure 31):
  - All cells fully saturated with a solution of the composition shown in Table 6.
  - The model starts with the condition of a breached and fully saturated waste package.
  - The spent fuel is assumed to be contacted by the in-package solution.
- The age of the fuel is assumed to be 1100 years out of reactor. Therefore, the model assumes that the waste package failed and was filled with solution 1000 years after emplacement and that the fuel was 100 years out of reactor when it was emplaced.
- The four alloys (Table 5) are congruently reacted with the solution composition given in Table 6 at the rates specified in Table 7.
- Geochemist's Workbench (as implemented in X1t) was used to determine the evolution of the pH, Eh and speciation (solution and solids) of the simulated in-package solution corresponding to a given set of steel dissolution rates.
- The amount of H<sub>2</sub> produced and its distribution with time over the reactive transport domain (through diffusion and advection) are determined and quantified as fugacity and molal concentrations.
- Results from the in-package solution simulations (i.e. H<sub>2</sub> concentrations) are used as input to the FMD model, which is then used to calculate the spent fuel degradation rate.
  - Parameter values for the fuel environment are from Jerden et al., 2015.

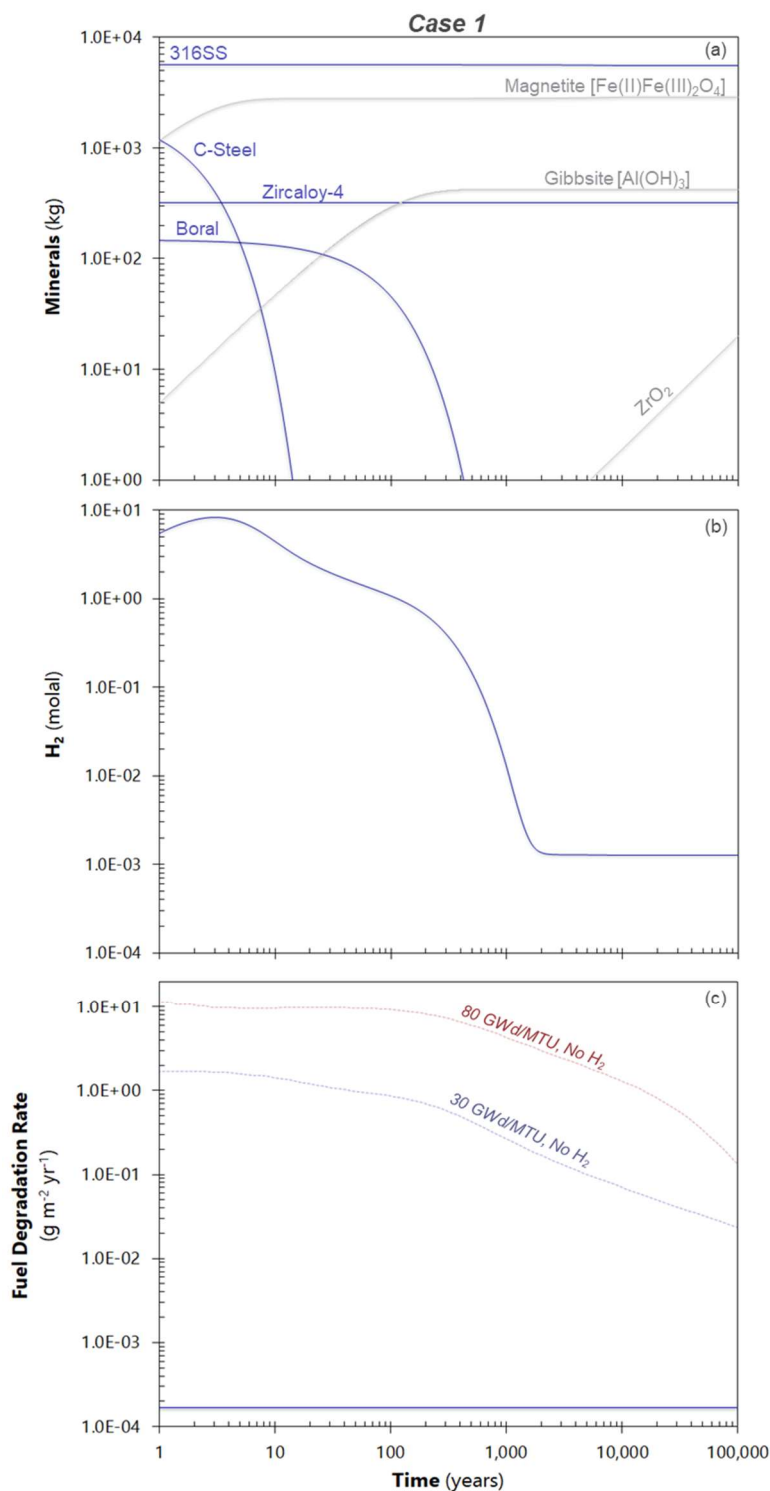
- Temperature was held constant at 25 °C for all runs.
  - Each model case included two fuel burnup values (30 GWd/MTU and 80 GWd/MTU) as indicated in the results shown below.
- The H<sub>2</sub> threshold concentrations for inhibiting oxidative fuel degradation is 1.0x10<sup>-3</sup> molal for 80 GWd/MTU and 1.0x10<sup>-4</sup> molal for 30 GWd/MTU.

Figure 32a shows the masses of the in-package alloys (blue) and the most abundant corrosion products (gray) over the simulation duration for Case 1 (Table 7). For these conditions (low Eh, High pH and relatively high NaCl concentrations) the model predicts that C-steel will be nearly completely corroded to magnetite around 20 years after the waste package has been breached and the aluminum alloy Boral will be nearly consumed approximately 400 years after the waste package breach. The production of around 10 kg of zirconium oxide indicates that a moderate amount of Zircaloy has corroded; however, most of the original alloy remains at the end of the simulation. Only minimal amounts (~100 grams) of 316 SS are predicted to corrode for the Case 1 model conditions.

The predicted in-package H<sub>2</sub> concentration for Case 1 is shown in Figure 32b. The initially high concentrations of over 1 molal are due to the sudden rise in H<sub>2</sub> fugacity caused by the relatively rapid corrosion of C-steel. Following the corrosion of C-steel and Boral the concentration reaches a long-term steady state concentration of 1.3x10<sup>-3</sup> molal. This steady state concentration is due to the continued production of H<sub>2</sub> by Zircaloy that persists throughout the 100,000-year time frame of the model. This concentration is higher than the threshold concentrations for inhibiting oxidative fuel degradation for both fuel burnup values (Figure 32c).

Modeling Cases 2 and 3 have the same alloy corrosion rates (Table 7) and thus show the same alloy mass loss and corrosion products production with time, as shown in Figure 33(a). The difference between Cases 2 and 3 and Case 1 is that the Zircaloy, 316SS and Boral corrosion rates are all lower due to the low chloride concentration condition for these runs (see Figures 29 and 30 above). As with Case 1 the rapid corrosion of C-Steel leads to its consumption 20 years after the waste package breach. Boral persists for around 4,000 years, a factor of 10 longer than for the Case 1 conditions (Figure 33a). The slower corrosion of Zircaloy is indicated by the lack of significant zirconium oxide production (Figure 33a).

The H<sub>2</sub> concentrations for Cases 2 and 3 show similar trends but are off-set due to the presence of advective solution transport in Case 3 (light blue line in Figure 33b). Advection causes lower H<sub>2</sub> concentrations as it transports H<sub>2</sub> produced by corrosion out of the waste package cell at a rate faster than diffusion. The points on the curves shown in Figure 33b are the thresholds for inhibiting oxidative dissolution for the two different fuel burnups. The higher burnup fuel produces more radiolytic oxidants and thus requires a higher H<sub>2</sub> concentration to counteract oxidation. The threshold concentrations are 1.0 millimolal H<sub>2</sub> for the 80GWd/MTU case and 0.1 millimolal for the 30GWd/MTU fuel. The H<sub>2</sub> concentrations drop below these thresholds around the time when nearly all of the Boral is consumed. The spent fuel degradation rate for Case 2 increases to the oxidative dissolution rate at around 3,000 years, while the degradation rate for Case 3 (light red line, Figure 33c) increases to the oxidative dissolution rate around 2,200 years after waste package breach. This difference is due to the lower H<sub>2</sub> concentrations caused by advection.



**Figure 30.** Results from the Case 1 model scenario (Table 7). The time axis refers to the time elapsed from the start of in-package corrosion (assumed to be 1000 years after emplacement). The fuel is assumed to be 1100 years old at time zero in these model runs. In the bottom plot (c), the solid line just below  $2 \times 10^{-4} \text{ g m}^{-2} \text{yr}^{-1}$  is the calculated degradation rate for the Case 1 scenario representing the chemical dissolution rate of the fuel. The dotted lines show the degradation rates calculated for cases with no  $\text{H}_2$  for a high burnup fuel (80 GWd/MTU) and a low burnup fuel (30 GWd/MTU).

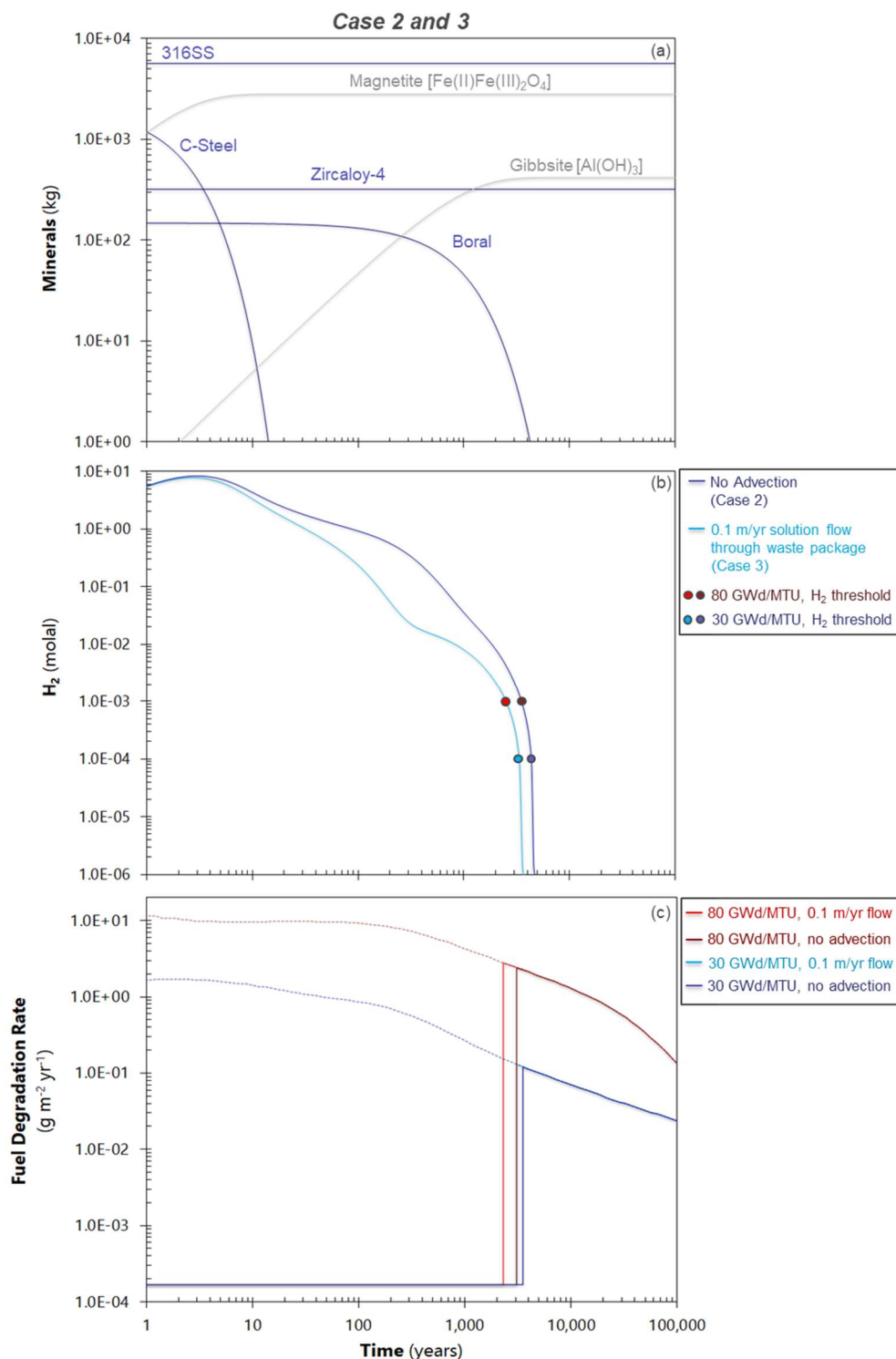


**Figure 31.** Results from the Case 2 and 3 model scenarios (Table 7). The time axis refers to the time elapsed from the start of in-package corrosion (assumed to be 1000 years after emplacement). The points in the middle plot (b) indicate the  $H_2$  concentration thresholds for inhibiting oxidative fuel dissolution for the two different fuel burnups. In the bottom plot (c), the solid line just below  $2 \times 10^{-4} g\ m^{-2}\ yr^{-1}$  is the calculated chemical dissolution rate of the fuel. The dotted lines show the degradation rates calculated for cases with no  $H_2$  for a high burnup fuel (80 GWd/MTU) and a low burnup fuel (30 GWd/MTU).



The results for modeling Cases 4 and 5 are shown in Figure 34. These Cases are for low Eh, high pH and low NaCl concentrations without and with advection respectively. The only difference between these Cases and Cases 3 and 4 are that the corrosion rate used for C-steel is considerably lower (see high pH, low NaCl empirical curve in Figure 29). For these runs the Boral is the first alloy to be consumed at around 4,000 years after the waste package breach, while the C-steel persists for the full 100,000-year model duration (Figure 34a). There is no significant corrosion of either 316SS or Zircaloy in these model cases.

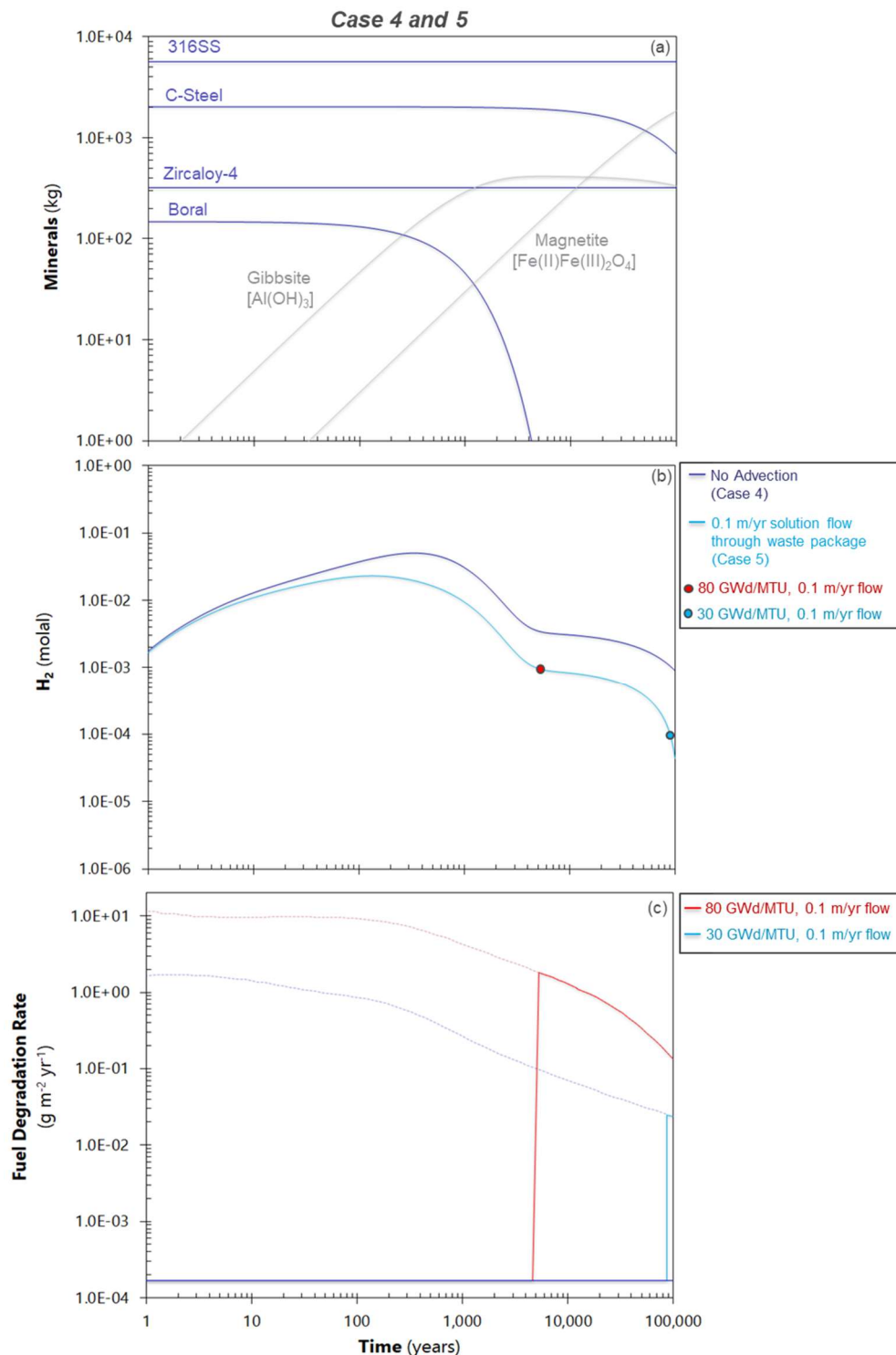
Approximately 1,000 kg of C-steel is corroded to magnetite during the Cases 4 and 5 runs, which leads to relatively high H<sub>2</sub> concentrations throughout the model time frame (Figure 34b). The Case 4 H<sub>2</sub> concentration remains above the threshold concentration for inhibiting oxidative fuel dissolution for 100,000 year; however, when advection is accounted for (Case 5) the H<sub>2</sub> concentrations drop below the threshold values at 4,200 years for the 80 GWd/MTU fuel and at 90,000 year for the 30 GWd/MTU fuel (Figures 34b and 34c).

Modeling Cases 6 and 7 are for low Eh, high pH and high NaCl conditions (Table 7) and are differentiated from Cases 4 and 5 by a somewhat higher corrosion rates for C-steel, 316SS and Zircaloy. As shown in Figure 35a, Boral is predicted to be the first alloy consumed at around 4,000 years and C-Steel is predicted to persist until around 70,000 years. The H<sub>2</sub> concentration for Case 6 (no advection) remains above the threshold for inhibiting oxidative fuel dissolution until around 30,000 years for the 80 GWd/MTU fuel and around 40,000 years for the 30 GWd/MTU fuel. For Case 7 (with advection) the H<sub>2</sub> concentration remains above the H<sub>2</sub> threshold until around 20,000 years for the 80 GWd/MTU fuel and around 30,000 years for the 30 GWd/MTU fuel (Figures 35b and 35c).

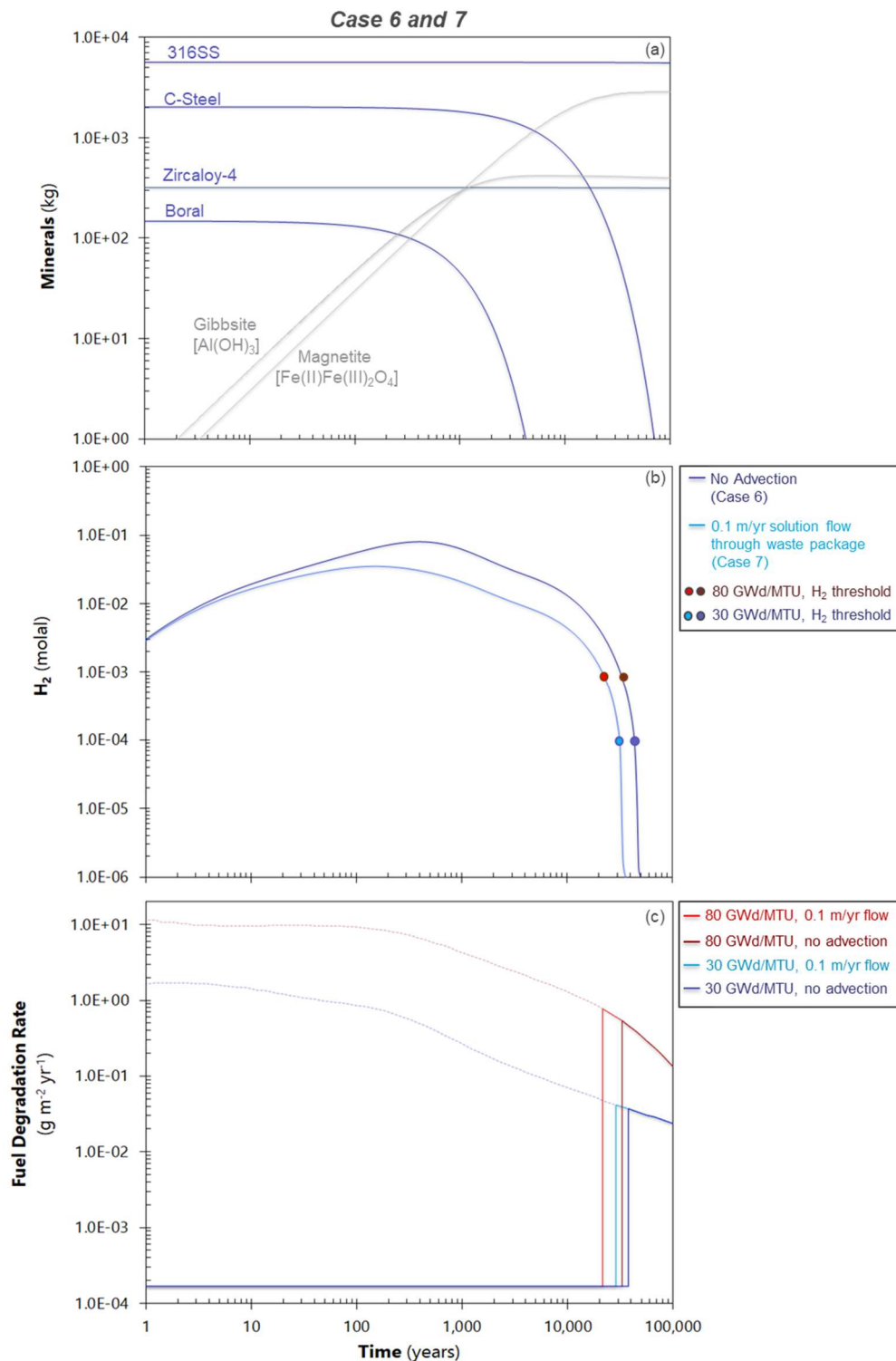
Case 8 is for high Eh, low pH and low NaCl concentration conditions and thus involves relatively high alloy corrosion rates (Table 7). For this Case, C-steel is predicted to be nearly completely consumed within 20 years after waste package breach while Boral is consumed by year 400 (Figure 36a). Both 316SS and Zircaloy show minor amounts of corrosion as evidenced by the production of magnetite, goethite and zirconium oxide relatively late in the simulation time (>10,000 years) (Figure 36a). The H<sub>2</sub> concentration for Case 8 decreases to below the H<sub>2</sub> thresholds for inhibiting oxidative fuel dissolution at around 1,500 years (Figure 36b and 36c). Including advection for this model run did not produce significantly different results as those shown in Figure 36.

Figure 37 shows the results for Case 9, which is for high Eh, low pH and high NaCl concentration conditions. This case differs from Case 8 by the higher 316SS corrosion rate used. For this run, in addition to the C-steel and Boral being consumed by 20 years and 400 years respectively, the 316SS is also consumed by around the 5,500-year mark of the simulation (Figure 37a). Minor Zircaloy corrosion is indicated by the production of approximately 10 kg of zirconium oxide. Following the consumption of most the 316SS the ferric oxyhydroxide Goethite begins to replace the primary iron corrosion phase magnetite. This is due to the relatively oxidizing conditions assumed for the seepage water (Table 7).

The resulting H<sub>2</sub> concentration for Case 9 falls below the thresholds for inhibiting oxidative fuel dissolution around the time that most of the 316SS is consumed (~5,000 years). Due to the steep decrease in the H<sub>2</sub> concentration, the time at which the two different burnup fuels commence oxidative dissolution are the same (Figures 37a and 37b). Advective transport through the waste package did not significantly change the results for Case 9.



**Figure 32.** Results from the Case 4 and 5 model scenarios (Table 7). The time axis refers to the time elapsed from the start of in-package corrosion (assumed to be 1000 years after emplacement). The points in the middle plot (b) indicate the  $\text{H}_2$  concentration thresholds for inhibiting oxidative fuel dissolution for the two different fuel burnups. In the bottom plot (c), the solid line just below  $2 \times 10^{-4} \text{ g m}^{-2} \text{ yr}^{-1}$  is the calculated chemical dissolution rate of the fuel. The dotted lines show the degradation rates calculated for cases with no  $\text{H}_2$  for a high burnup fuel (80 GWd/MTU) and a low burnup fuel (30 GWd/MTU).



**Figure 33.** Results from the Case 6 and 7 model scenarios (Table 7). The time axis refers to the time elapsed from the start of in-package corrosion (assumed to be 1000 years after emplacement). The points in the middle plot (b) indicate the  $H_2$  concentration thresholds for inhibiting oxidative fuel dissolution for the two different fuel burnups. In the bottom plot (c), the solid line just below  $2 \times 10^{-4} g\ m^{-2}\ yr^{-1}$  is the calculated chemical dissolution rate of the fuel. The dotted lines show the degradation rates calculated for cases with no  $H_2$  for a high burnup fuel (80 GWd/MTU) and a low burnup fuel (30 GWd/MTU).

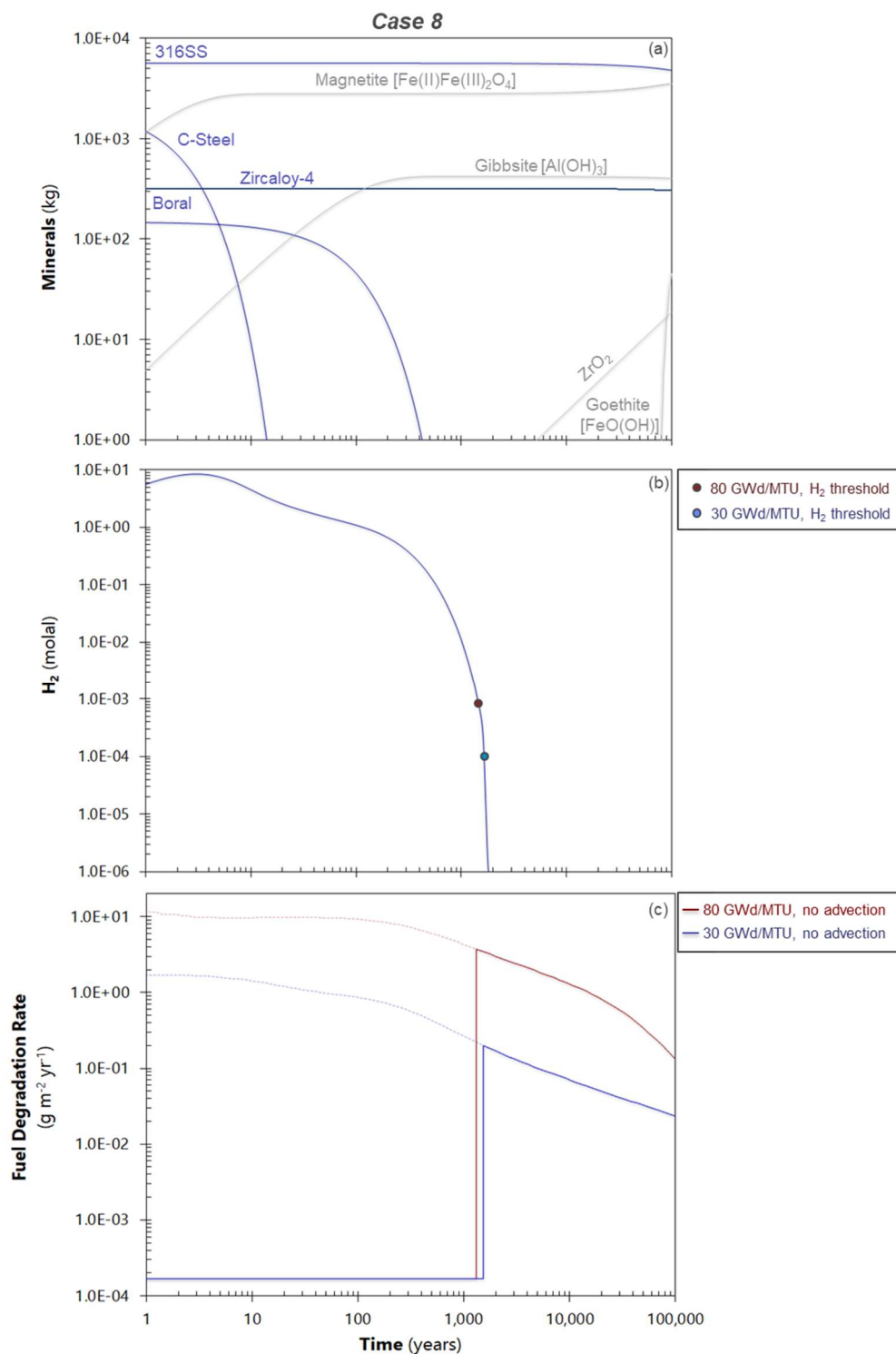


**Figure 34.** Results from the Case 8 model scenario (Table 7). The time axis refers to the time elapsed from the start of in-package corrosion (assumed to be 1000 years after emplacement). The points in the middle plot (b) indicate the  $\text{H}_2$  concentration thresholds for inhibiting oxidative fuel dissolution for the two different fuel burnups. In the bottom plot (c), the solid line just below  $2 \times 10^{-4} \text{ g m}^{-2} \text{yr}^{-1}$  is the calculated chemical dissolution rate of the fuel. The dotted lines show the degradation rates calculated for cases with no  $\text{H}_2$  for a high burnup fuel (80 GWd/MTU) and a low burnup fuel (30 GWd/MTU).

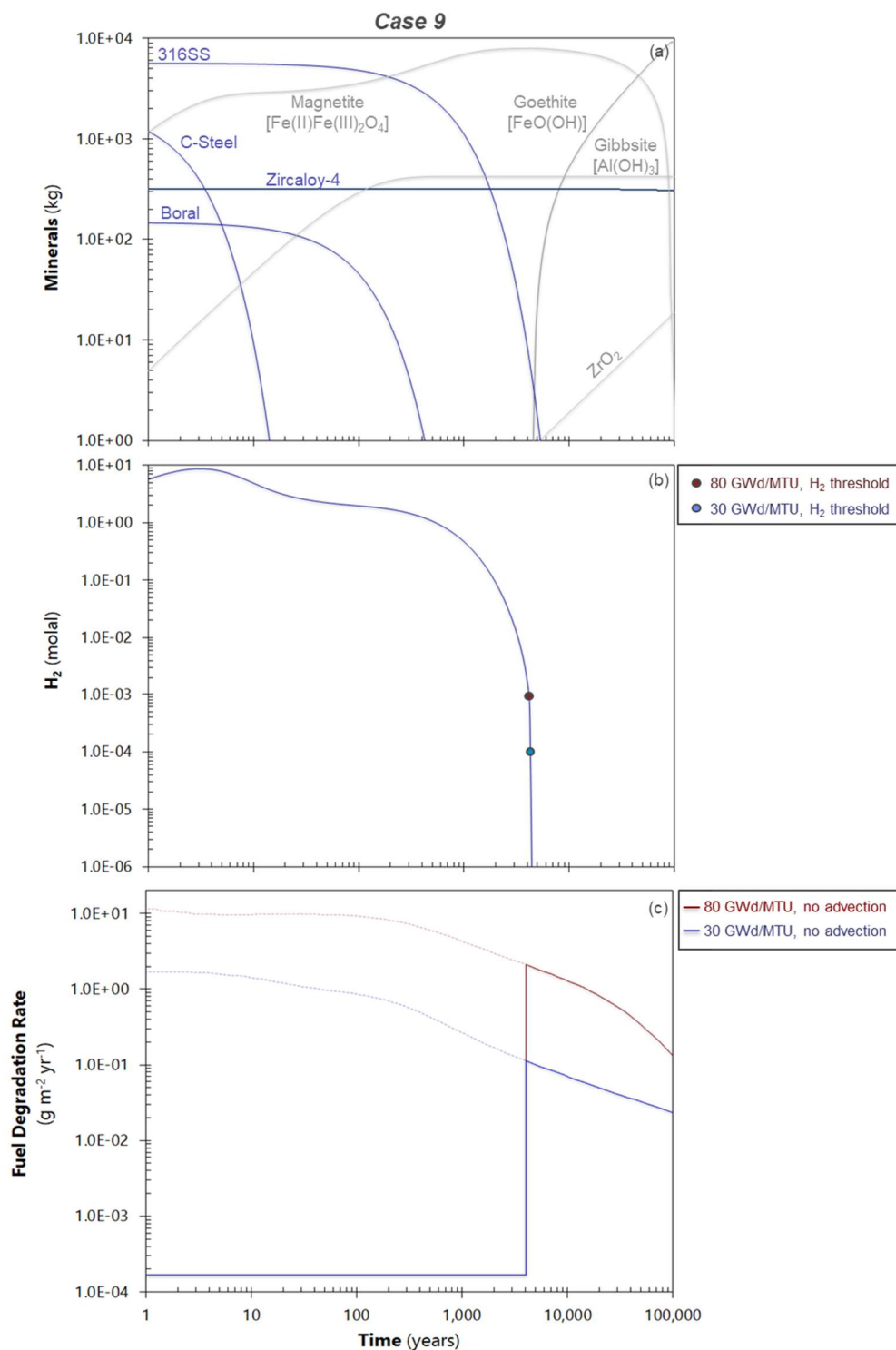


**Figure 35.** Results from the Case 9 model scenario (Table 7). The time axis refers to the time elapsed from the start of in-package corrosion (assumed to be 1000 years after emplacement). The points in the middle plot (b) indicate the  $\text{H}_2$  concentration thresholds for inhibiting oxidative fuel dissolution for the two different fuel burnups. In the bottom plot (c), the solid line just below  $2 \times 10^{-4} \text{ g m}^{-2} \text{ yr}^{-1}$  is the calculated chemical dissolution rate of the fuel. The dotted lines show the degradation rates calculated for cases with no  $\text{H}_2$  for a high burnup fuel (80 GWd/MTU) and a low burnup fuel (30 GWd/MTU).

## 5. CONCLUSIONS AND FUTURE WORK

### 5.1 Conclusions

This report presents new results from a series of electrochemical corrosion tests that provide information needed to parameterize the fuel matrix degradation (FMD) model and an associated prototype in-package chemistry (IPC) model. The data provide corrosion rates for the major in-package alloys over a range of relevant pH and redox conditions. The alloys tested are: 316L stainless steel (316SS), AISI 4320 carbon steel (C-steel), Zircaloy-4 and the borated aluminum composite material Boral. The range of conditions were: pH 4, 7 and 10, salt concentrations ranging from nanomolal to around one molal and several relevant potentials (see Tables 1 – 3). All tests were performed at laboratory ambient temperatures ( $\sim 22^{\circ}\text{C}$ ). These electrochemical tests provide new insights into the corrosion behavior of these in-package alloys that traditional mass loss tests (coupon immersion) do not provide. The primary findings are as follows:

- Based on the trend lines shown in Figure 29, the corrosion rates for the carbon steel and Boral samples in millimolal salt solutions increase by a factor of approximately 10 over the relevant potential range of  $-0.6\text{ V}$  to  $0.6\text{ V}$  (vs SHE). At higher salt concentrations (0.1 molal) carbon steel shows a dramatic increase in its corrosion rate ( $\sim 6$  orders of magnitude) over this potential range.
- The corrosion rate of carbon steel decreases from values greater than  $1 \times 10^5\text{ g m}^{-2}\text{ yr}^{-1}$  for all tests performed in millimolal (or greater) salt concentrations down to around  $30\text{ g m}^{-2}\text{ yr}^{-1}$  in tests run at the lowest salt concentration (around 1 nanomolal).
- Boral showed evidence of non-uniform corrosion at potentials greater than  $0.24\text{ V}$  (vs SHE) (Figures 14).
- Based on the trend lines shown in Figure 30, the corrosion rate of 316 stainless steel tested in pH 7 and 10, millimolal salt solutions increases dramatically (by 7 orders of magnitude) over the relevant potential range of  $-0.6\text{ V}$  to  $0.6\text{ V}$  (vs SHE). The increase in 316 stainless steel corrosion rates in tests performed in pH 4, millimolal salt solutions is less steep over this potential range (increasing by around 3 orders of magnitude) but yields higher corrosion rates at lower potentials (Figure 30).
- The trend line for Zircaloy in Figure 30 indicate that its corrosion rate increases by approximately 2 orders of magnitude over the relevant potential range of  $-0.6\text{ V}$  to  $0.6\text{ V}$  (vs SHE).

The corrosion rates measured in electrochemical tests with individual alloys were used as direct input to demonstrate the coupled in-package chemistry (IPC) – fuel matrix degradation (FMD) model that is being developed to provide long-term spent fuel degradation rates as chemical conditions (Eh, pH, speciation) evolve within a breached waste package. The combined prototype IPC and FMD model discussed in Jerden et al., 2019 and this report has been updated in the current study to account for the new alloy corrosion rate data. The coupled fuel degradation/IPC model links the FMD mixed potential code with the reactive transport code X1t, which is a module within the Geochemist's Workbench (GWB) software package. The reactive transport model consists of a 1D domain discretized with 21 reaction diffusion cells and includes a single waste package cell, two cells within the bentonite backfill and then 19 other cells within the near-field host rock.

The concentration of dissolved  $\text{H}_2$  is the key variable in the FMD model, therefore, being able to accurately model the evolution of  $\text{H}_2$  within the waste package is essential for accurately predicting long-term spent fuel degradation rates. The prototype X1t, IPC model has been used successfully to calculate the amount of  $\text{H}_2$  produced and accumulated within a breached waste package due to the corrosion of stainless steel, carbon steel, Boral and Zircaloy and the results are discussed above. The experimental results for individual

alloys were used to exercise the model for a set of 9 new model cases (Table 7). This model uses the masses, surface areas and corrosion rates of each alloy to calculate the  $H_2$  generation rate and tracks all relevant chemical speciation reactions to provide information on in-package pH, Eh and chemistry for a  $10^5$ -year generic repository simulation. The model includes both the diffusive and advective transport of dissolved  $H_2$  away from the waste package to track the concentration over time.

The sensitivity runs performed with this combined prototype IPC - FMD model using the new in-package alloy corrosion data presented above resulted in the following observations:

- For model runs using the corrosion results from tests performed in pH 4 solutions, the in-package carbon steel is predicted to be consumed by corrosion within 20 years of the waste package being breached. This rapid corrosion causes a sharp maximum in  $H_2$  fugacity and concentration. The concentration of  $H_2$  does not decrease rapidly following the consumption of carbon steel due to  $H_2$  production by the relatively rapidly corroding Boral materials.
- Boral is predicted to persist for around 400 years under high Eh conditions and for around 4,000 years under low Eh conditions. Boral is the major source of  $H_2$  in model cases with rapid carbon steel consumption and slow stainless steel and Zircaloy corrosion (Cases 2 and 3, Figure 33).
- In most cases stainless steel and Zircaloy are predicted to persist for over 100,000 years after the waste package has been breached. This is due to their low corrosion rates as measured in the electrochemical experiments (below  $0.01 \text{ g m}^{-2} \text{ yr}^{-1}$ ). These alloys do produce  $H_2$  as they slowly corrode, but the rate is too low to maintain the  $H_2$  concentration above the threshold for inhibiting oxidative dissolution of the fuel for most cases. The exception being Case 1 where a stainless steel corrosion rate of  $1 \text{ g m}^{-2} \text{ yr}^{-1}$  leads to a  $H_2$  production rate that maintains the concentration below the oxidative dissolution threshold for the duration of the model time frame (Figure 33).
- The relatively low corrosion rates for stainless steel and Zircaloy (below  $1 \text{ g m}^{-2} \text{ yr}^{-1}$  for all cases except one) lead to their persistence through the 100,000-year time frame for the simulations. These alloys produced  $H_2$  throughout the model runs; however, the amount produced is small.
- Including a pore water advection rate of 0.1 m/yr through the waste package cell decreases the  $H_2$  concentration by a factor of approximately 4. This leads to  $H_2$  concentrations dropping below the threshold needed to inhibit oxidative dissolution of the fuel under some conditions (e.g., see Case 5, Figure 34).
- Under high Eh conditions, the model predicts that the in-package  $H_2$  concentration will have a steep increase corresponding to the rapid corrosion of carbon steel and Boral during the first 400 years following the waste package breach, but will fall below the threshold for inhibiting oxidative fuel dissolution by approximately 1,500 years due to  $H_2$  diffusion out of the waste package cell.

The results of this study confirm the conclusions and recommendations that were identified and discussed in Jerden et al., 2017, Jerden et al., 2018 and Jerden et al., 2019. Several of the information gaps identified in those studies remain, but the present study has demonstrated how electrochemical testing methods can be used to address the key information gaps. Clearly, the environmental dependencies of in-package alloy corrosion rates must be taken into account in the FMD model to represent the evolving conditions in a breached waste package. Electrochemical measurements of alloy corrosion rates provide values and dependencies on T, Eh, pH, and  $Cl^-$  conditions for active corrosion and after passivation and thus are essential for source term model parameterization and validation. However, the effects of Galvanic coupling



on the long-term corrosion rates and analytical functions for the pH and chloride ion concentration effects remain to be determined. Also, galvanic coupling of fuel and alloys (particularly Zircaloy) must be assessed.

## 5.2 Future Work

The primary information gaps that still need to be filled to reduce uncertainties in long-term spent fuel degradation and associated radionuclide source term modeling include the following:

- Corrosion rates for galvanically coupled alloys and fuel remain to be measured.
- A robust waste package breaching model based on reliable electrochemical measurements such as those described in this report, is needed to determine the time at which spent fuel degradation initiates. This is particularly important for high burnup fuels that will produce high concentrations of radiolytic oxidants if contacted by water at times less than 1000 years out of the reactor. The threshold concentration of  $H_2$  needed to inhibit oxidative dissolution will be higher for “young” fuels relative to older fuels.
- The mechanism by which  $H_2$  inhibits the oxidative dissolution of spent fuel remains uncertain. The mechanism is currently modeled in the FMD model as a catalytic process by which  $H_2$  oxidation is energetically promoted on the surface of the Ru-epsilon phase particles (see Figure 3 above and Broczkowski et. al., 2005). However, other processes may also influence the  $H_2$  effect on fuel dissolution such as the destruction of radiolytic oxidants (e.g.,  $H_2O_2$ ) by  $H_2$  within the solution near the degrading fuel surface. Electrochemical tests performed on simulated spent fuel (e.g., lanthanide and noble metal doped  $UO_2$ ) could be used to address this issue.
- Relatedly, any processes that counteract the mechanism by which  $H_2$  suppresses oxidative fuel degradation need to be accounted for. There is some evidence that halides (particularly Br) may be capable of poisoning the catalytic properties of the Ru-epsilon phase particles (Metz et. al., 2008), although the process is not fully understood or quantified. Electrochemical tests on simulated noble metal particle bearing fuel could be used to address this issue.
- It is also important that any processes that consume  $H_2$  within the breached waste package be quantified and taken into account in the IPC – FMD model. Two key processes known to consume  $H_2$  that have not yet been fully quantified experimentally or included in the IPC model are microbial oxidation of  $H_2$  (e.g., Bagnoud et al., 2016) and the chemical conversion of  $H_2$  to sulfur species such as  $H_2S$ ,  $HS^-$ ,  $S^{2-}$ . These processes could lead to higher fuel degradation rates by decreasing  $H_2$  concentrations within the breached waste package and need to be understood and quantified.

The use of tailored electrochemical methods such as those discussed in this report offer the most accurate and versatile means for quantifying the long-term degradation behavior of spent fuel because its primary degradation mechanism is electrochemical in nature. Future studies should build on the existing alloy corrosion database and electrochemical modeling techniques to fill the data gaps identified above.



## 6. REFERENCES

- Bard, A., Faulkner, L., "Electrochemical methods: Fundamentals and Applications", John Wiley and Sons, Inc., 2001
- Bagnoud, A., Leupin, O., Schwyn B., Bernier-Latmani R., Rates of microbial hydrogen oxidation and sulfate reduction in Opalinus Clay rock, *Applied Geochemistry* 72 (2016) 42-50
- Broczkowski, M. E.; Noël, J. J.; Shoesmith, D. W., "The inhibiting effects of hydrogen on the corrosion of uranium dioxide under nuclear waste disposal conditions" *Journal of Nuclear Materials*, vol. 346, pp. 16-23, 2005.
- Buck E., Jerden, J., Ebert, W., Wittman, R., "Coupling the Mixed Potential and Radiolysis Models for Used Fuel Degradation," FCRD-UFD-2013-000290, 2013.
- Buck, E., Mausolf, E., McNamara, B., Soderquist, C., Schwantes, J., "Nanostructure of Metallic Particles in Light Water Reactor Used Nuclear," *Journal of Nuclear Materials*, vol. 61, pp. 236–243, 2015.
- Bethke, C.M., Yeakel, S. "The Geochemist's Workbench User's Guides, Version 10.0," Aqueous Solutions LLC, Champaign, Illinois, 2014.
- CRWMS M&O 2003, "In-Package Chemistry Abstraction," ANL-EBS-MD-000037 REV 02., Las Vegas, Nevada: CRWMS M&O. ACC: MOL.20000418.0818, 2003.
- Energy Solutions, "Generic Design for Small Standardized Transportation, Aging and Disposal Canister Systems," DOE Advisory and Assistance Services Contract Task Order 18, UPDATED FINAL REPORT, May 14, 2015, 317 p.
- Fillmore, D.L., "Parameter Selection for Department of Energy Spent Nuclear Fuel to be Used in the Yucca Mountain License Application, Idaho National Engineering and Environmental Laboratory Report," INEEL/EXT-03-01032 Revision 1, October 2003
- Gattu, V. K., Ebert, William L., Tehrani, N., Indacochea, J. E. "Electrochemical Measurements of Steel Corrosion for Modeling H<sub>2</sub> Generation." CORROSION 2018. NACE International, 2018.
- Grambow, B., Bruno, J., Duro, L., Merino, J., Tamayo, A., Martin, C., Pepin, G., Schumacher, S., Smidt, O., Ferry, C., Jegou, C., Quiñones, J., Iglesias, E., Rodriguez Villagra, N., Nieto, J., Martínez-Esparza, A., Loida, A., Metz, V., Kienzler, B., Bracke, G., Pellegrini, D., Mathieu, Wasselin-Trupin, G., Serres, C., Wegen, D., Jonsson, M., Johnson, L., Lemmens, K., Liu, J., Spahiu, K., Ekeröth, E., Casas, I., de Pablo, J., Watson, C., Robinson, P., Hodgkinson, D., "Model Uncertainty for the Mechanism of Dissolution of Spent Fuel in Nuclear Waste Repository," European Commission, Final Report for MICADO Project, EUR 24597, 2010.
- Jerden, J., Lee, E., Gattu, V., Ebert, W., "Fuel Matrix Degradation Model Development Update: Alloy Corrosion Rates and Hydrogen Generation", Report for Spent Fuel and Waste Science and Technology Project, Milestone #: M4SF-19AN010301013, ANL/CFCT-19/12, September 30, 2019
- Jerden, J., Lee, E., Gattu, V., Ebert, W., "Results from In-Package Alloy Electrochemical Corrosion Experiments: Implications for Long-Term Spent Fuel Degradation", Report for Spent Fuel and

- Waste Science and Technology Project, Milestone #: M3SF-19AN010301012, ANL/CFCT-19/2, March 19, 2018
- Jerden, J., Gattu, V, Ebert, W., “Update on Validation and Incorporation of a New Steel Corrosion Module into Fuel Matrix Degradation Model”, Report for Spent Fuel and Waste Science and Technology Project, Milestone #: M4SF-18AN010301017, August 6, 2018
- Jerden, J., Frey, K., Ebert, W., “Spent Fuel Matrix Degradation and Canister Corrosion: Quantifying the Effect of Hydrogen”, Report for Spent Fuel and Waste Science and Technology Project, Report #: SFWD-SFWST-2017-000039, February 28, 2017
- Jerden J., Hammond, G., Copple J., Cruse, T., Ebert W., “Fuel Matrix Degradation Model: Integration with Performance Assessment and Canister Corrosion Model Development,” FCRD-UFD-2015-000550, July 21, 2015
- Jerden J. Frey K. Ebert W., “A Multiphase Interfacial Model for the Dissolution of Spent Nuclear Fuel, *Journal of Nuclear Materials*, vol. 462, pp. 135–146, 2015.
- Johnson J, Anderson F, Parkhurst DL. Database thermo.com.V8.R6.230, Rev 1.11. Lawrence Livermore National Laboratory, Livermore, California; 2000
- Johnson, L.H. and F. King, “Canister options for the disposal of spent fuel,” Nagra Technical Report 02-11, 2003.
- Kaesche, H., “Metallic Corrosion,” National Association of Corrosion Engineers International, Houston, TX, 1985.
- King F. and Kolar M., “Mathematical Implementation of the Mixed-Potential Model of Fuel Dissolution: Model Version MPM-V1.0,” Ontario Hydro, Nuclear Waste Management Division Report No: 06819-REP-01200-10005 R00, 1999.
- King F. and Kolar M., “The Mixed-Potential Model for UO<sub>2</sub> Dissolution MPM Versions V1.3 and V1.4,” Ontario Hydro, Nuclear Waste Management Division Report No. 06819-REP-01200-10104 R00, 2003.
- King, F., “Overview of a Carbon Steel Container Corrosion Model for a Deep Geological Repository in Sedimentary Rock,” Nuclear Waste Management Organization Report TR-2007-01, March 2007, 71 p.
- Laaksoharju M., Smellie, J., Tullborg, E-L., Gimeno, M., Hallbek, L., Molinero, J., Waber, N., “Bedrock hydrogeochemistry Forsmark site descriptive modeling SDM-Site Forsmark,” SKB R-Report (R-08-47), SKB, Stockholm, Sweden, 2008.
- Metz V., Loida A., Bohnert E., Schild D., Dardenne K., “Effects of Hydrogen and Bromide on the Corrosion of Spent Nuclear Fuel and  $\gamma$ -irradiated UO<sub>2</sub>(s) in NaCl Brine,” *Radiochim. Acta* 96, 637–648, 2008.
- Miller, W.M., W.R. Alexander, N.A. Chapman, I.G. McKinley, and J.A.T. Smellie, “Natural analogue studies in the geological disposal of radioactive wastes,” *Studies in Environmental Sciences* 57, Elsevier, Amsterdam (also Nagra Technical Report NTB 93-03), 1994.

- Ollila, K., "Dissolution of Unirradiated UO<sub>2</sub> and UO<sub>2</sub> Doped with <sup>233</sup>U in Low- and High-Ionic-Strength NaCl Under Anoxic and Reducing Conditions," Posiva Working Report 2008-50, 2008.
- Pastina B., and LaVerne, J. A. "Effect of Molecular Hydrogen on Hydrogen Peroxide in Water Radiolysis", *Journal of Physical Chemistry A* 105, 9316-9322, 2001.
- Posiva, "Safety case for the disposal of spent nuclear fuel at Olkiluoto – Design Basis 2012," Eurajoki, Finland: Posiva Oy. POSIVA 2012-03. ISBN 978-951-652-184-1, 2012.
- Radulescu, G., "Repository Science/Criticality Analysis," Oak Ridge National Laboratory, Reactor and Nuclear Systems Division, FTOR11UF0334, ORNL/LTR-2011, Oak Ridge National Laboratory, Oak Ridge, TN., 2011.
- Röllin S., Spahiu K., Eklunda U., "Determination of Dissolution Rates of Spent Fuel in Carbonate Solutions Under Different Redox Conditions with a Flow-through Experiment," *Journal of Nuclear Materials*, vol. 297, pp. 231–243, 2001.
- Shoesmith, D., Kolar, M., King, F., "A Mixed-Potential Model to Predict Fuel (Uranium Dioxide) Corrosion within a Failed Nuclear Waste Container" *Corrosion*, vol. 59, pp. 802-816, 2003.
- Shoesmith, D., "The Role of Dissolved Hydrogen on the Corrosion/Dissolution of Spent Nuclear Fuel," Nuclear Waste Management Organization, Toronto, Ontario, Canada, TR-2008-19, November 2008.
- Simpson, J.P. 1989, "Experiments on canister materials for Swiss high- level waste disposal projects, Part IV. National Cooperative for the Storage of Radioactive Waste Technical Report," NAGRA-NTB-89-19, 1989.
- Turnbull, A. 2009, "A Review of the Possible Effects of Hydrogen on Lifetime of Carbon Steel Nuclear Waste Canisters NAGRA," Technical Report 09-04, July 2009.
- Wang Y. et al., "Used Fuel Disposal in Crystalline Rocks: Status and FY14 Progress," FCRD-UFD-2014-000060, SAND2014, Sandia National Laboratories, Albuquerque, NM., 2014.